



Title	Multi-scale Structural Evaluation Method of Reinforced Concrete Member under the Effect of Frost Damage
Author(s)	WANG, Zhao
Citation	北海道大学. 博士(工学) 甲第13794号
Issue Date	2019-09-25
DOI	10.14943/doctoral.k13794
Doc URL	http://hdl.handle.net/2115/79177
Type	theses (doctoral)
File Information	WANG_Zhao.pdf



[Instructions for use](#)

**Multi-scale Structural Evaluation Method of Reinforced Concrete
Member under the Effect of Frost Damage**

凍害を受けた鉄筋コンクリート部材の
マルチスケール構造性能評価法

By

Zhao WANG

A thesis submitted in partial fulfilment of the requirements for the degree of
Doctor of Philosophy in Engineering

Professor Tamon UEDA
Supervisor

Division of Engineering and Policy for Sustainable Environment
Graduate School of Engineering
Hokkaido University
September 2019

ACKNOWLEDGEMENT

At beginning, I would like to express my sincerest thanks and gratitude to my supervisor - Professor Tamon Ueda, for his guidance and support of five years during both my master's and doctoral studies. His valuable lectures, accurate instructions and kind suggestions have given me enormous help towards my research. Besides, I have learnt from him not only the technical knowledge but also the attitude as a researcher.

Secondly, I would like to express my great thanks to my seniors in our research team: Dr. Dawei Zhang, Dr. Fuyuan Gong and Dr. Yi. Wang. They generously shared their time and knowledge with me from where I could get many inspired ideas. Appreciations are extended to all my lab mates, especially Saeid Mehrpay, Liangliang Wei, Miaochang Zhu and Yang Xie for the enjoyable days with them. In addition, many thanks to Dr. Pengru Deng and Su Wang who are always helpful and enthusiastic friends.

I would also like to express my sincere thanks to my examination committee members: Professor Takashi Matsumoto, Professor Takafumi Sugiyama and Dr. Koji Matsumoto for their vital comments and questions which has further improved the contents of my study. Special thanks are given to Dr. Hiroshi Furuuchi and Hiroshi Hayashida for the valuable instructions on conducting experiments.

Sincere gratitude is extended to Werawan Manakul, Natalya Shmakova and all the stuff of e3 program for their kind and patient help during my life in Hokkaido University. Great thanks also go to Professor Zhimin Wu and Professor Licheng Wang for giving me tremendous support ever since I was undergraduate student.

Finally, I am extremely grateful to my parents and my wife for the endless encouragement and unconditional love. It is your faith in me that help me struggle through those hard times.

ABSTRACT

Frost damage is one the most important durability issues for reinforced concrete structures built in cold and wet areas. Once frost damage initiates, cracks are induced and enlarged in concrete which leads to severer strength and stiffness reduction. Besides, the bond between concrete and reinforcement bars is also weakened due to the degradation of concrete cover and concrete-reinforcement interface. As a result, the structural behaviors usually show significant deterioration and the lifetime of structures is shortened under the effect of frost damage. Thus, to predict and evaluate the reinforced concrete structural performance under frost damage is urgently needed so that effective maintenance and repairment could be proposed.

In fact, several scales exist for the fundamental mechanisms of frost action to the structural performance with frost damage: (1) pore pressures owing to ice formation initiate in microscale which accounts for the propagation of meso-cracks in concrete; (2) the meso-cracks result in the macroscopic residual deformation of concrete, strength and stiffness reduction of concrete and deteriorated bond properties; (3) the degradation of concrete material and bond in macroscale material level is further upscaled into structural level to affect the structural performance. This study has developed a multi-scale evaluation methodology for reinforced concrete structures under the effect of frost damage following the above-mentioned “material (micro-meso-macro)-structure” system.

The methodology starts from explaining the mechanism of frost action in the porous skeleton. Both strengthening effect of elastic properties due to ice-filled pores and damaging effect by meso-cracks due to internal pressures are considered by implementing the comprehensive strengthening/damaging models into the mesoscopic simulation application – RBSM (Rigid Body Spring Model). 2D RBSM is adopted for the meso-macro simulation of concrete with frost damage while axisymmetric RBSM is newly developed to simulate the bond degradation. Based on the parametric study of simulation results, macroscale deterioration constitutive models of material and bond are proposed, and various experimental data are used to verify the models. The deterioration constitutive models are further upscaled and integrated into the 3D structural analysis with FEM (Finite Element Method). The structural behaviors of

reinforced concrete beam are analyzed with this methodology and experiments are conducted to demonstrate its applicability.

Keywords: frost damage, reinforced concrete structure, meso-macro simulation, structural analysis, rigid body spring model, finite element method

TABLE OF CONTENTS

ACKNOWLEDGEMENT	i
ABSTRACT	ii
TABLE OF CONTENTS	iv
1. Introduction.....	1
1.1 Background	1
1.2 Statement of Problems and Objectives.....	2
1.3 Outline of the Dissertation	7
References	9
2. Theoretical Background in Micro and Meso Scale.....	12
2.1 2D Mesoscale Plane Stress RBSM.....	12
2.2 Micro-meso Strengthening/Damaging Model.....	15
2.2.1 Ice content evaluation.....	16
2.2.2 Internal pressures and ice strengthening effect	18
2.2.3 Mesoscale constitutive relationships for springs.....	20
References	22
3. Meso-macro Simulation and Modeling of Concrete.....	24
3.1 Simulation Models	24
3.2 Simulation Results.....	26
3.2.1 Residual strain and meso-cracks after FTC.....	26
3.2.2 Degradation of compressive behaviors	27
3.2.3 Degradation of tensile behaviors.....	32
3.3 Modeling of Deteriorated Constitutive Relationships.....	34
3.3.1 Compressive stress-strain curve	34
3.3.2 Tensile stress-strain curve	36
3.4 Conclusions of This Chapter	38
References	39
4. Meso-macro Simulation and Modeling of Bond	41
4.1 Axisymmetric Mesoscale RBSM	41
4.1.1 Basic concepts	41

4.1.2	Development of stiffness matrix	42
4.2	Verification of Axisymmetric RBSM	45
4.2.1	Uniaxial compression of concrete	45
4.2.2	Uniaxial tension of reinforcement	49
4.2.3	Bond-slip of pulling-out specimens	51
4.3	Simulation and Modeling of Bond	58
4.3.1	Meso-macro simulation	58
4.3.2	Modeling of deteriorated bond-slip relationship	59
4.4	Conclusions of This Chapter	60
	References	62
5.	Macroscale Structural Analysis	64
5.1	Finite Element Analysis	64
5.1.1	2D heat transfer analysis	64
5.1.2	3D reinforced concrete beam model	66
5.1.3	Material models	66
5.1.4	Bond-slip models	69
5.2	Experimental Verification	70
5.2.1	Specimens preparations	70
5.2.2	FTC and loading	72
5.3	Results and Discussions	73
5.3.1	Ultrasonic pulse velocity	73
5.3.2	Structural behaviors	75
5.4	Conclusions of This Chapter	78
	References	80
6.	Conclusions	81
	Appendix-A	83
	Appendix-B	84

Chapter 1

1. Introduction

1.1 Background

In cold and regions, frost damage is a very common and serious durability issue for reinforced concrete structures. It is generally believed that frost damage is attributed to the ice formation from water inside the porous materials, e.g. mortar, concrete, etc. Once temperature falls below the freezing point (lower than 0 °C due to the super cooling effect as Gruebl 1980) of pore water, ice initiates and causes tensile stress on the porous skeleton. The stress is usually high enough to result in micro-cracks, which reduces the strength and stiffness of concrete. As the key mechanism of reinforced concrete structure, bond ability between reinforcement bars and concrete also deteriorates under the effect of frost damage. One reason is above-mentioned degradation of concrete, and the other reason is that the bond region between reinforcement and concrete can be also treated as porous substance with larger pore fraction. Thus, ice will also form in the bond interface and cause tensile stress to tear apart the connect between rebars and concrete. Combining both aspects, the reinforced concrete structures suffer severe damage under frost action, and the structural morphology as well as performance might change greatly (Hayashida et al. 2014). For instance, **Fig. 1.1** shows some concrete structures which has suffered frost damage and have obvious deterioration: **Fig. 1.1(a)** shows that the concrete parts of a bridge which has suffered frost action show severe cracking and even spalling off; **Fig. 1.1 (b)** shows that the roof top of a concrete-made building with frost damage has obvious scaling phenomenon; **Fig. 1.1 (c)** shows that the fence made of concrete has pop-out appearance under the effect of frost damage.



(a) cracking



(b) scaling



(c) Pop out

Fig. 1.1. Examples of typical frost damage cases

1.2 Statement of Problems and Objectives

Deterioration of mechanical properties of concrete:

Frost damage is an important durability issue to concrete materials that has been studied for several decades. Many experimental investigations are available on the mechanical behaviors of frost-damaged concrete: Shi et al. (1997) investigated the compressive strength, tensile strength and elastic modulus with cylindrical concrete specimens which suffered the freezing-thawing cycles (FTC) as suggested by ASTM C666-84. Obvious reduction in these characteristics was observed for the frost-damaged specimens. Hasan et al. (2004) conducted “air-freezing and water-thawing” FTC tests with concrete prisms and proposed an empirical stress-strain model for frost-damaged concrete using residual plastic tensile strain as the damage index. Shang and Song (2006) followed GBJ82-85 FTC test standard to conduct both uniaxial and biaxial loading test with frost-damaged concrete. Duan et al. (2011) carried out uniaxial compressive experiments with unconfined and confined prismatic concrete specimens following the same standard as Shang and Song (2006). Based on the test results, the degradation models were proposed where FTC numbers were used as the damage index. Through scanning electron microscopy technique, Zou et al. (2008) successfully observed the micro-structures of the frost-damaged concrete. Besides, a material degradation model was also proposed based on their test results in which relative dynamic elastic modulus (RDEM) was chosen as the damage index. Cao et al. (2013) suggested to use both FTC number and RDEM as the frost damage indexes and proposed an empirical deterioration constitutive relationship based on the experimental data. Diao et al. (2011) studied the combined effect of steel corrosion,

FTC and sustained load on structural performance of RC beams to find faster and severe degradation took place in coupled damage factors including frost damage. Although Diao et al. (2011) referred to the same test standard (GBJ82-85), the minimum temperature of each cycle in Diao et al. (2011)'s test was more than two times lower than that in Shang et al. (2006) and Duan et al. (2011). Peterson et al. (2007) referred to RILEM TC 176-IDC standard, which was a different FTC method compared with the above ones. In their test, only one surface of the specimen was open to freezing-thawing environment. The effects of FTC on elastic modulus of concrete and interfacial bond behaviors were evaluated. Hanjari et al. (2011) adopted the temperature variation suggested by RILEM TC 176-IDC but chose to submerge the specimen during FTC. Both compressive and tensile degradation of concrete were evaluated, as well as the bond properties after FTCs. All the previous experimental conditions were briefly summarized in **Table 1.1**.

As observed in **Table 1.1**, the test parameters such as concrete mix proportions (e.g. water/cement ratio), number of FTCs and minimum temperature of each cycle varied a lot by different papers. Though some empirical equations (Hasan et al. 2004, Duan et al. 2011, Cao et al. 2013, etc.) were proposed to model the mechanical degradation of concrete, the models were somehow limited to specific test conditions and difficult to be adopted in general. Besides, from those test results with air-entrained concrete (Shi et al. 1997, Hasan et al. 2002, 2004, Zou et al. 2008), quite different results were obtained where some experiments showed almost no strength and stiffness reduction while others showed significant reduction. Current work focuses on the non-AE case for following reasons: (1) the effectiveness of AEA is very sensitive to its type and quality; (2) frost damage has also been found in many structures even air-entraining-agent was adopted which yields the effects of AEA is minimal in those structures; (3) a practical deterioration model for non-AE concrete is still absent and in urgent need.

Table 1.1. Summarization of available experimental studies on frost-damaged concrete

	Standard	Size (mm ³)	FTC exposure (°C)	No. of FTCs	<i>w/c</i>	Comp. strength (MPa)	Air void (%)	Measured properties ^{*1}
Shi (1997)	ASTM C666-84	Φ100x203	10→-30 (5 hrs)	0, 30, 60, 90	0.35	61.71	/ (AE)	<i>f_c</i> , <i>E</i> , <i>ν</i> , <i>f_{ts}</i> , <i>τ_{ss}</i> , <i>G</i>
			Min.=−30 (3 hrs)			59.85		
			−30→10 (4 hrs)		0.48	43.37		
						38.63		
Hasan (2004)	ASTM C666-03	100x100x200	20→-25 (1 hr in air ^{*2})	0, 88, 148, 188	0.60	47.8	4.5 (AE)	<i>ε_{pf}</i> , <i>f_c</i> , <i>E</i> , <i>ε_{c0}</i>
			Min.=−25 (3 hrs in air)					
			−25→15 (1 hr in air)					
			15→20 (2 hrs)					
Hasan (2002)	ASTM C666-97	100x100x400 100x100x100	4.4~−17.8	0, 34, 62, 109, 205, 261, 305	0.50	<i>f_t</i> =4.43	/(AE)	RDEM, <i>f_t</i> , <i>E</i> , <i>w_{max}</i> , <i>G_f</i>
				0, 10, 17, 28, 41, 76, 205, 305		<i>f_t</i> =4.20	(Non-AE)	
Zou (2008)	ASTM C666-03	100x100x400	/	0, 100, 150, 200, 250, 300	0.38	42.98	(AE)	<i>f_c</i> , <i>E</i> , <i>ε_{c0}</i>
Shang (2006)	GBJ82-85	100x100x100	6→-15 (2.5-3 hrs)	0, 25, 50, 75	0.50	34.2	1.7	RDEM, Δ <i>W</i> ,
			−15→6 (2.5-3 hrs)					<i>f_{ts}</i> , <i>f_c</i> , <i>E</i> , <i>ε_{c0}</i>
Fu (2010)	GBJ82-85	100x100x400	8→-17 (1-2 hrs)	0, 25, 50,	0.35	50.7	/ (Non-AE)	RDEM, Δ <i>W</i> , <i>f_c</i> , <i>f_{ts}</i> , <i>f_t</i>
		150x150x150	−17→8 (1-2 hrs)	75, 100, 125	0.39	45.4		
					0.46	35.6		
					0.58	29.1		
Duan (2011)	GBJ82-85	100x100x300	8→-17 (3.5 hrs)	0, 50, 75, 100, 125, 150, 175, 200	0.48	41.54	/ (Non-AE)	<i>f_c</i> , <i>E</i> , <i>ε_{c0}</i> , <i>a</i> , <i>b</i>
			−17→8 (3.5 hrs)		0.54	39.18		
					0.60	28.73		
Ji (2007)	GBJ82-85	100x100x100	8→-17 (3 hrs)	0, 15, 30, 50	0.5	33.98	1.9	<i>f_c</i> , <i>E</i> , <i>ε_{c0}</i> , <i>f_{ts}</i>
		150x150x150	−17→8 (3 hrs)			30.71		
Cao (2013)	GBJ82-85	150x150x150	8→-17 (1.5 hrs)	0, 25, 50, 75, 100, 125	0.41	50.7	3.0	RDEM, <i>f_c</i> , <i>E</i> , <i>ε_{c0}</i> , <i>a</i> , <i>b</i>
					0.44	45.4	3.4	
			−17→8 (1.5 hrs)		0.55	35.6	2.6	
					0.75	29.1	3.0	
Diao (2011)	GBJ82-85	100x100x300	20→-35 (2 hrs)	0, 50, 100, 150, 200	0.44	41.30	/ (Non-AE)	<i>f_c</i> , <i>E</i>
			−35→20 (2 hrs)		0.50	26.59		
					0.55	26.48		
Peterson (2007)	RILEM TC 176-IDC	75x80x250	/	/	0.6	/	1.0	RDEM, <i>E</i>
							1.5	
							1.5	
Hanjari (2011)	RILEM TC 176-IDC	Φ100x200	/	/	0.57	40.97	/(Non-AE)	RDEM, <i>f_c</i> , <i>E</i> , <i>ε_{c0}</i> , <i>f_{ts}</i> , <i>w_{max}</i>

Note:

*¹- f_c : compressive strength, E : Elastic modulus, ε_{c0} : compressive peak strain, f_{ts} : splitting tensile strength, f_t : pure tensile strength, τ_s : shear strength, G : shear modulus, RDEM: relative dynamic elastic modulus, ΔW : weight loss, w_{max} : maximum crack width, G_f : fractural energy, a and b : parameters in Guo et al. (2003)'s compressive stress-strain model;

*²-The FTC exposure is “water condition” in default unless “in air” is specifically marked;

*³-The air void shown in only number represents “Non-AE” condition;

Besides those experimental works, theoretical studies have also been accomplished to explain the frost damage mechanism of concrete materials: In the beginning, it was believed that the hydraulic pressure caused frost damage. Powers (1949) developed the hydraulic pressure model on basis of Darcy's law which was a time-dependent approach. In his model, maximum spacing factor of the entrained air could be determined to prevent frost damage. Recent studies found that the crystallization and cryosuction pressures were another mechanism since frost damage could also be found in partially saturated cases, which could hardly be explained by Powers' theory since the hydraulic pressure vanished. Sun et al. (2010) developed a mathematical way to calculate the overall stress and strain caused by crystallization and cryosuction pressures. Coussy and Monteiro (2008) also developed a static model based on poro-mechanics without considering the hydraulic pressure theory. Both Sun and Monteiro ignored the hydraulic flow and pressure release which meant the internal forces were same during each cycle as long as the specimen is sealed. However, it could only be adopted for the first few cycles since the permeability would increase with damage accumulation, which made the water movement more easily and the pressure might release. Gong et al. (2015) proposed a comprehensive model combining both Powers' model and poro-mechanical model where the internal pressure during FTC was determined by various environmental factors such as water cement ratio, minimum temperature, etc. The internal pressure model was also implemented into 2D mesoscale RBSM program to simulate the deformability of mortar and concrete under frost action. The simulation results correlated well with both open and close test, which strongly demonstrated its reliability.

In this paper, meso-macro simulation will be conducted on mechanical behaviors of

concrete under the effect of frost damage based on the above-mentioned program. Three environmental parameters are adopted including water cement ratio (w/c), minimum temperature of each FTC and number of FTC. A prediction model of compressive strength of frost-damaged concrete will be developed with verification by the available experimental data. In addition, the constitutive relationships including compressive stress-strain and tensile stress-crack width of frost-damaged concrete will also proposed depending on both simulation results and several test data. The proposed models are further utilized in analyzing the structure performance of RC structures under FTC conditions through FEM applications.

Deterioration of bond properties:

Different like the study of mechanical deterioration of frost-damaged concrete, very limited attention has been given to the degradation of bond properties. Experiment especially pulling-out test with specimens of short embedment length could be found which investigated the local bond-slip relationship under the effect of frost damage. Shih et al. (1988) conducted concentric pulling-out test with prismatic specimens to find that the cyclic temperature change affected both bond strength and bond-slip curve. Peterson et al. (2007) carried eccentric pulling-out test on cubic specimens with only one-surface suffering frost damage according to the RILEM TC 176 IDC test standard. Their results showed that the bond strength decreased but the slip at peak bond stress showed slightly decreasing for the first few cycles and then increased. By contrast, other experiments indicated continuous increase of slip at peak bond stress and reduction of bond strength with accumulation of frost damage (Hanjari et al. 2011, Xu et al. 2017, Ji 2007, etc.). Liu et al. (2016) proved that the bond between reinforcement and TIC (thermal insulation concrete) had a better resistance against frost damage than normal concrete due to the special porous structures of TIC. Xu et al. (2017) tested the frost-damaged bond properties under monotonic and cyclic loading and proposed empirical formulas.

Theoretical or simulation studies are hard to find relating to the frost-damaged bond behaviors. The reasons could be due to the complexity of bond mechanism and frost damage mechanism. However, with the internal pressure model (Gong et al. 2015) and mesoscale RBMSM, it is possible to develop an analytical tool to simulate and evaluate the bond deterioration under the effect of frost action. Since bond action between concrete and deformed bars is a three-dimensional issue where hoop stresses in concrete exist to resist the outward

component of the interactive pressure between rebar and concrete. The 2D mesoscale plane stress/strain RBSM (Nagai et al. 2004) program could no longer be applied. 3D RBSM program (Nagai et al. 2005) could simulate the bond behaviors properly but consume numerous time due to the large number of elements in mesoscale, especially for the calculation time of frost damage procedure (Gong et al. 2017). Therefore, the axisymmetric mesoscale Rigid Body Spring Method will be developed to avoid the extremely large consumption of calculation time.

In this study, the axisymmetric mesoscale RBSM program is aimed to be exploited to investigate the bond degradation under frost damage. Similarly, only non-air entrained case was focused. Firstly, the newly-developed axisymmetric RBSM needs verification by uniaxial compression test of concrete and uniaxial tension of rebar. Afterwards, one-way pulling-out test will be simulated after a whole process of FTC. The simulated bond-slip relationships for both sound (non-damaged) and damaged specimens are compared with previous experiments to prove its reliability and applicability of the program. Finally, parametric study is conducted to propose a meso-macro simulation-based deterioration model of bond-slip relationship, which will be adopted in the numerical structural analysis of reinforce concrete members.

Structural performance of frost-damaged RC beam:

Once the deterioration is modeled for concrete and bond, structural analysis will be executed to investigate the degradation of structural performance under the effect of frost damage. Since the thermal lag effect exists so the damage level varies according to different locations (Wang et al. 2017), 2D heat transfer analysis is conducted so that the material and bond constitutive models can be given by positions of the RC beam. Non-linear structural analysis using DIANA FEA is achieved and experiment is also prepared to verify the proposed multi-scale methodology. Till now, the multi-scale structural evaluation methodology can be summarized as: microscale model of ice strengthening/damaging effect→application into mesoscale RBSM→meso-macro simulation of concrete and bond degradation→macroscale constitutive models of frost-damaged concrete and bond→integrating into FEM→structural analysis.

1.3 Outline of the Dissertation

Chapter 1 presents the background of the study with some engineering examples. The research objectives are stated in three aspects: deterioration of concrete, bond and structural behaviors

under the effect of frost damage. The clear scope of developing the multi-scale structural evaluation method is mentioned.

Chapter 2 describes the basic concept of 2D mesoscale plane-stress RBSM and ice strengthening/damaging model. The microscale enhanced elastic properties are considered in the mesoscale springs of RBSM and internal pressure by ice formation is acted as pre-stress in the springs.

Chapter 3 contains the meso-macro simulations where the uniaxial compression and pure tension test of frost-damaged concrete is simulated by the program and macroscale constitutive laws are modeled with the simulation results. The constitutive models are also verified with existing test data.

Chapter 4 focuses on developing the axisymmetric mesoscale RBSM with applying rebar element so that the bond-slip behavior could be simulated. The new RBSM program is verified by simulation of uniaxial compression of concrete and uniaxial tension of rebar. Pulling-out test is then simulated, and macroscale bond-slip constitutive laws are modeled with the meso-macro simulation results.

Chapter 5 combines the results from last two chapters and includes 2D heat transfer analysis for RC beam. The material and bond deterioration models are applied in the 3D structural analysis with FEM approach. The flexural behaviors of RC beam are evaluated, and experimental work is done to check the reliability of the proposed multi-scale method.

Chapter 6 summarizes the work and draw conclusions of this study.

References

- P. Gruebl, Rapid ice formation in hardened cement paste, mortar and concrete due to supercooling, *Cement and Concrete Research*. 10 (1980) 334-345.
- H. Hayashida, Structural property evaluation of freeze-thaw-damaged RC beam members by nonlinear finite-element analysis, 4th International Conference on the Durability of Concrete Structures. West Lafayette. (2017).
- S. Shi, Effect of freezing-thawing cycles on mechanical properties of concrete, *China Civil Engineering Journal*. 30 (4) (1997) 35-42.
- American Society for Testing and Materials Committee, Standard test method for resistance of concrete to rapid freezing and thawing (ASTM C666-84), 1987 Annual Book of ASTM Standards. 4 (2) (1987).
- M. Hasan, H. Okuyama, H. Sato, T. Ueda, Stress-strain model of concrete damaged by freezing and thawing cycles, *Journal of Advanced Concrete Technology*. 2 (1) (2004) 89-99.
- H. Shang, Y. Song, Experimental study of strength and deformation of plain concrete under biaxial compression after freezing and thawing cycles, *Cement and Concrete Research*. 36 (10) (2006) 1857-1864.
- National standard of The People's Republic of China, Standard test methods for long term performance and durability of ordinary concrete (GBJ82-85), Peking: China Architectural and Building Press. (1986).
- A. Duan, W. Jin, J. Qian, Effect of freeze-thaw cycles on the stress-strain curves of unconfined and confined concrete, *Materials and Structures*. 44 (7) (2011) 1309-1324.
- C. Zou, J. Zhao, F. Liang, Stress-strain relationship of concrete in freeze-thaw environment, *Frontiers of Architecture and Civil Engineering in China*. 2 (2) (2008) 184-188.
- D. Cao, L. Fu, Z. Yang, X. Qin, Study of constitutive relations of compresses concrete subjected to action of freezing-thawing cycles, *Journal of Building Materials*. 16 (1) (2013) 17-23.
- B. Diao, Y. Sun, S. Cheng, Y. Ye, Effects of mixed corrosion, freeze-thaw cycles, and persistent loads on behavior of reinforced concrete beams, *Journal of Cold Regions Engineering*. 25 (1) (2011) 37-51.
- L. Peterson, L. Lohaus, M.A. Polak, Influence of freezing-and-thawing damage on behavior of

reinforced concrete elements, *ACI Materials Journal*. 104 (4) (2007) 369-378.

M. J. Setzer, Capillary suction, internal damage and freeze-thaw test-reference method and alternative methods A and B (RILEM TC 176 IDC), *Materials and Structures*. 34 (9) (2001) 515-525.

K.Z. Hanjari, P. Utgenannt, K. Lundgren, Experimental study of the material and bond properties of frost-damaged concrete, *Cement and Concrete Research*. 41(3) (2011) 244-254.

M. Hasan, K. Nagai, Y. Sato, T. Ueda, Tensile stress-crack model for plain concrete damaged by freezing and thawing action, *Proceedings of Japan Concrete Institute*. 24 (2) (2002) 109-114.

L. Fu, Experimental study on the strength of concrete under uniaxial tensile load after freeze-thaw cycles, Master Dissertation. Yangzhou University (2010).

X. Ji, The experimental study and theoretical analysis on the mechanical performance of concrete and bond behavior between concrete and steel bar after freezing and thawing, Doctoral Dissertation. Dalian University of Technology (2007).

Z. Guo, X. Shi, Reinforced concrete theory and analysis, Beijing: Tsinghua University Press. (2003).

T.C. Powers, The air requirement of frost resistant concrete, *Proceedings of Highway Research Board*, 29 (1949) 184-211.

Z. Sun, G.W. Scherer, Effect of air voids on salt scaling and internal freezing temperatures, *Cement and Concrete Research*. 40 (2) (2010) 260-270.

O. Coussy, P.J. Monteiro, Poroelastic model for concrete exposed to freezing temperatures, *Cement and Concrete Research*. 38 (1) (2008) 40-48.

F. Gong, E. Sicat, D. Zhang, T. Ueda, Stress analysis for concrete materials under multiple freeze-thaw cycles, *Journal of Advanced Concrete Technology*. 13 (3) (2015) 124-134.

T.S. Shih, G.C. Lee, K.C Chang, Effect of freezing cycles on bond strength of concrete, *Journal of Structural Engineering*. 114 (3) (1988) 717-726.

S. Xu, A. Li, H. Wang, Bond properties for deformed steel bar in frost-damaged concrete under monotonic and reversed cyclic loading, *Construction and Building Materials*. 148 (2017) 344-358.

X. Ji, Y. Song, Y. Liu, Effect of freeze-thaw cycles on bond strength between steel bars and concrete, *Journal of Wuhan University of Technology-Mater. Sci. Ed.* 23 (4) (2008) 584-588.

- Y. Liu, F. Chen, W. Wang, Z. Li, Bond performance of thermal insulation concrete under freeze-thaw cycles, *Construction and Building Materials*. 104 (2016) 116-125.
- K. Nagai, Y. Sato, T. Ueda, Mesoscopic simulation of failure of mortar and concrete by 2D RBSM, *Journal of Advanced Concrete Technology*. 2 (3) (2004) 359-374.
- K. Nagai, Y. Sato, T. Ueda, Mesoscopic simulation of failure of mortar and concrete by 3D RBSM, *Journal of Advanced Concrete Technology*. 3 (3) (2005) 385-402.
- F. Gong, T. Ueda, Y. Wang, D. Zhang, Z. Wang, Mesoscale simulation of fatigue behavior of concrete materials damaged by freeze-thaw cycles, *Construction and Building Materials*. 144 (2017) 702-716.
- Z. Wang, F. Gong, D. Zhang, H. Hayashida, T. Ueda, Mesoscale simulation of concrete behavior with non-uniform frost damage with verification by CT imaging, *Construction and Building Materials*. 157 (2017) 203-213.

Chapter 2

2. Theoretical Background in Micro and Meso Scale

2.1 2D Mesoscale Plane Stress RBSM

The RBSM (Rigid Body Spring Method) is a discrete numerical analysis method firstly developed by Kawai in 1978. It has been widely accepted that RBSM is a more proper way pertaining to simulate the cracking issues for cementitious materials compared with the continuum applications such as Finite Element Method or Finite Difference Method. Several researches have been conducted to develop the RBSM to simulate mechanical behaviors and durability issues of reinforced concrete structures:

Kawai firstly introduced the concept and made several discussions based on the simulation results of 2D plane stress/strain RBSM programs. Bolander and Saito (1998) adopted truss reinforcement elements and polyhedron concrete elements and applied the approach to analyze reinforced concrete beams. Muto et al. (2004) implemented 2D in-plane reinforcement elements with configuring the outline of ribs and simulated uniaxial pulling-out test of specimens with long embedment length. Tension stiffening was successfully observed in their simulation and the effect of several parameters were also discussed. Nagai et al. (2004, 2005) developed the 2D mesoscale plane stress/strain as well as 3D mesoscale RBSM for concrete materials by introducing mortar elements, coarse aggregate elements and the interfacial transition zone (ITZ) between mortar and aggregate. Using the mesoscopic programs, the uniaxial/biaxial mechanical tests and the bending test for concrete and mortar were simulated. Nakamura et al. (2006) and Wang et al. (2011) combined truss element with 2D in-plane RBSM to simulate the mass transfer in cracks and deterioration of concrete with chloride ion penetration. Hayashi et al. (2017) adopted 3D concrete elements and reinforcement elements with geometric shape to conduct pulling-out simulation to investigate the RC anchorage performance with 3D RBSM. Ueda et al. (2009) proposed a mesoscale stress-strain relationship for concrete under the effect of frost damage on basis of the 2D mesoscale plane stress RBSM. Meso-macro simulations were conducted where the results showed satisfactory agreement with experiments. Through integrating the theoretical internal pressure models due to ice formation as well as the constitutive models of springs accounting for frost action and fatigue, Gong et al. (2015a)

developed the 2D mesoscale plane stress RBSM application to simulate the monotonic and fatigue behaviors of frost-damaged concrete which was demonstrated by several experiment results. In current study, 2D mesoscale plane stress RBSM is adopted to simulate and model the compressive and tensile behaviors of frost-damaged concrete.

In the 2D mesoscale plane stress RBSM program, the analytical model is divided into polyhedron elements which are randomly arranged using Voronoi diagram to assure that cracks could take place in random directions. Each Voronoi cell stands for a mortar or aggregate element and two adjacent elements are connected by a couple of normal and shear springs. Each element has two translational and one rotational degrees of freedom at the center of gravity, see **Fig. 2.1**. The values of stiffness for normal and shear springs are calculated as Eq. (2.1) where a weighted average value is used in case the springs represent mortar-aggregate interfaces. In Eq. (2.1), K_n and K_s mean the stiffness of normal and shear springs; h_i is the length of the perpendicular line from the centroid of element to the boundary, see **Fig. 2.1**; Naming K_{sp} to be the stiffness with subscripts n and s standing for normal and shear springs, respectively. The values of K_{sp} could be given as Eq. (2.2), where E_{elem} and ν_{elem} are the mesoscopic elastic modulus and Poisson's ratio of the element (mortar or aggregate) which are derived from the macroscale material values, see Eq. (2.3) (Nagai et al. 2004).

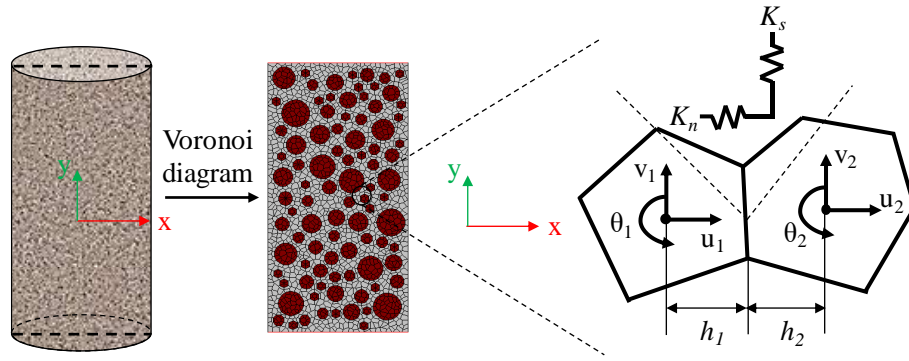


Fig. 2.1. Schematic diagram of 2D mesoscale plane stress RBSM

$$\begin{cases} K_n = \frac{K_{sp_{n1}}h_1 + K_{sp_{n2}}h_2}{h_1 + h_2} \\ K_s = \frac{K_{sp_{s1}}h_1 + K_{sp_{s2}}h_2}{h_1 + h_2} \end{cases} \quad (2.1)$$

$$\begin{cases} Ksp_n = \frac{E_{elem}}{(1-\nu_{elem})(1+\nu_{elem})} \\ Ksp_s = \frac{E_{elem}}{1+\nu_{elem}} \end{cases} \quad (2.2)$$

$$\begin{aligned} \nu_{elem} &= 20\nu^3 - 13.8\nu^2 + 3.8\nu \\ E_{elem} &= E(-8\nu_{elem}^3 + 1.2\nu_{elem}^2 - 0.2\nu_{elem} + 1) \end{aligned} \quad (2.3)$$

As suggested by Nagai et al. (2004), a normal distribution is assumed for the tensile strength of normal springs since concrete is a heterogeneous material, see Eq. (2.4). In which, $f_{t,elem}$ is the tensile strength of the element and assuming $f_{t,elem}=0$ for $f_{t,elem}<0$; μ is the average value of $f_{t,elem}$ while s is the standard derivation. For shear springs, an elasto-plastic behavior is adopted where the maximum shear strength τ_{max} is calculated on basis of the state of normal springs, as shown in Eq. (2.5):

$$f(f_{t,elem}) = \frac{\exp\left[-(f_{t,elem} - \mu)^2 / 2s^2\right]}{\sqrt{2\pi}s} \quad (2.4)$$

$$s = -0.2\mu + 1.5$$

$$\tau_{max} = \pm \left(0.11 f_{t,elem}^3 (-\sigma + f_{t,elem})^{0.6} + f_{t,elem} \right) \quad (2.5)$$

in which σ is the normal stress. For the springs of mortar-aggregate interfaces (ITZ), the shear criterion follows:

$$\tau_{max} = \pm (\sigma \tan \theta + c_i) \quad (2.6)$$

where θ and c_i are constant values. When the shear sliding is large enough and the attached length is significantly reduced, the shear stress could decrease. Besides, the shear strength and stiffness could also be affected by the tensile crack width in normal direction. This phenomenon is considering by applying Eq. (2.7) (Gong et al. 2017):

$$\begin{aligned} \tau_{max}' &= \tau_{max} (1 - \delta_s / l_{elem}) (1 - w / w_{max}) \\ K_s' &= K_s (1 - \delta_s / l_{elem}) (1 - w / w_{max}) \end{aligned} \quad (2.7)$$

where δ_s and l_{elem} are the sliding distance and length of attaching boundary between the adjacent elements; w is the crack width in normal direction and w_{max} is the maximum crack width for different components. In addition, the tensile stress could also be affected by the shear sliding and a linear reduction is adopted for normal springs in the program as below:

$$\begin{aligned} f_{t,elem}' &= f_{t,elem} (1 - \delta_s / l_{elem}) \\ K_n' &= K_n (1 - \delta_s / l_{elem}) \end{aligned} \quad (2.8)$$

The macroscopic material properties are input referring to the previous researches where some values have been proved to be related with others (Nagai et al. 2004). If one parameter is given, the rest ones could be calculated, see Eq. (2.9).

$$\begin{cases} E_m = 1000 [7.7 \ln(f_{cm}') - 5.5] \\ f_{tp} = 1.4 \ln(f_{cm}') - 1.5 \\ c/w = 0.047 f_{cm}' + 0.5 \\ c_i = -2.6w/c + 3.9 \\ f_{ti} = -1.44w/c + 2.3 \end{cases} \quad (2.9)$$

where f_{cm} is the compressive strength of mortar; E_m is the elastic modulus of mortar; f_{tp} is the pure tensile strength of mortar; f_{ti} is the tensile strength of ITZ; w/c is the water cement ratio and c_i is the parameter in interface criterion, see Eq. (2.6). Eq. (2.9) yields that ITZs have lower strength than mortar since f_{ti} is always less than f_{tp} .

2.2 Micro-meso Strengthening/Damaging Model

In the 2D mesoscale plane stress RBSM program, mechanical models are required in mesoscale which account for the concrete behaviors, especially under the effect of FTC (freezing and thawing cycles). The main influences from the ice formation are explained in the following statements by separating the influencing scale into microscale and mesoscale. At microscale level, the representative volume elements (RVE) are adopted which compose of cement matrix and pore space filled with ice, liquid and air, see **Fig. 2.2**. In this stage, the internal pore pressure is transferred into an equivalent volumetric force while the pore ice leads to higher elastic mechanical properties such as elastic modulus, Poisson's ratio and strength. At mesoscale level, springs connecting the Voronoi elements are adopted where the internal pore pressure is treated as pre-stressed condition and the ice-enhanced properties are directly considered in the constitutive laws. In this stage, meso-cracks form in normal springs if the ice volume expansion is big.

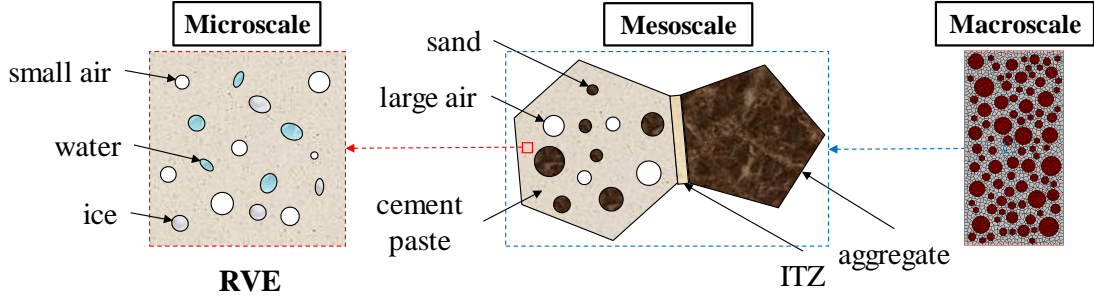


Fig. 2.2. Upscale of 2D mesoscale plane stress RBSM (Gong et al. 2018)

2.2.1 Ice content evaluation

Ice content is a very important factor to evaluate the frost damage of cementitious materials. In order to accurately estimate the ice content, the freezing point of pore water and pore size distribution of the porous materials should be known.

The freezing points of water in pores with specific radius (r_0) could be calculated based on Eq. (2.10) where $\gamma_{CL} \approx 0.04 \text{ J/m}^2$ is the specific energy of crystal/liquid surface; $\Delta S_f \approx 1.2 \text{ J/cm}^3\text{K}$ is the molar entropy of fusion; T_0 is for certain freezing temperature in Kelvin unit; $\delta \approx 0.9 \text{ nm}$ is the thickness of liquid film between the ice crystal and the pore wall (Scherer 2005).

$$r_0 = -\frac{2\gamma_{CL}}{T_0 \Delta S_f} + \delta \quad (2.10)$$

In previous studies, the authors have proposed an empirical pore size distribution model based on the water adsorption test by Xi et al. (1994). The model considers a wide range of parameters such as water/cement ratio, curing age and curing temperature etc., as shown in Eq. (2.11):

$$\begin{aligned} V(r \geq r_0) &= \frac{(W_{sat} - W(r_0)) / \rho_{wat}}{1 / \rho_{solid} + W_{sat} / \rho_{wat}} \\ &= \frac{1 / \rho_{wat}}{1 / \rho_{solid} + W_{sat} / \rho_{wat}} \cdot \left\{ W_{sat} - \frac{CkV_m(RH)}{[1 - k(RH)][1 + (C-1)k(RH)]} \right\} \end{aligned} \quad (2.11)$$

where $V(r \geq r_0)$ means the absolute volume of pores with larger radius than r_0 in unit volume of cement paste; W_{sat} stands for the normalized water content by weight of cement paste; ρ is the density of substance; RH is the relative humidity; The values of W_{sat} and RH could be calculated

as Eq. (2.12) where $\gamma_{LV} \approx 0.072 \text{ J/m}^2$ is the specific energy of liquid/vapor surface; $v_l = 1.8 \times 10^{-5} \text{ m}^3/\text{mol}$ is the molar volume of water; $R = 8.314 \text{ J/K/mol}$ is the ideal gas constant; the thickness of adsorbed liquid-like layer $\delta' = 10^{-9}(0.834RH + 0.0626 + 0.02309(1.105 - RH)^{-1})$. The other parameters are given in Eq. (2.13) based on Xi et al. (1994).

$$W_{sat} = \frac{CkV_m}{(1-k)(1+(C-1)k)} \quad (2.12)$$

$$RH = \exp\left(-\frac{2\gamma_{LV}}{r_0 - \delta'} \frac{v_l}{RT}\right)$$

$$\begin{cases} V_m = 0.9 \left(0.068 - \frac{0.22}{t} \right) \left(0.85 + 0.45 \frac{w}{c} \right) \\ k = \frac{(1-1/n)C-1}{C-1} \\ n = 1.1 \left(2.5 + \frac{15}{t} \right) \left(0.33 + 2.2 \frac{w}{c} \right) \\ C = \exp\left(\frac{855}{T}\right) \end{cases} \quad (2.13)$$

In Eq. (2.13), t is the curing age; T is the curing temperature in absolute unit and w/c is the water cement ratio. Combining Eq. (2.10) and (2.11), the ice content at a certain temperature could be calculated by integrating the normalized pore size distribution $v(r \geq r_0)$, see Eq. (2.14).

$$\psi_c(T_0) = \int_{r_0}^{\infty} v(r) dr = \int_{-2\gamma/(T_0 \Delta S_{fv}) + \delta}^{\infty} v(r) dr \quad (2.14)$$

To consider and quantify the phenomenon of hysteresis between freezing and thawing, the pore shape factor is adopted since the freezing point is usually controlled by the size of pore entry while the thawing point is usually controlled by the size of pore body. The pore shape factor ζ could be approximately regressed by the minimum temperature of FTC as $\zeta = -0.0095T_{\min} + 0.125$ according to Gong et al. (2015b) based on Sun and Scherer (2010)'s tests. The thawing curve is modified as following: in the relationship between ice content and temperature, if temperature has reached the minimum T_{\min} and starts to increase, the existing ice will not melt immediately but melt until the temperature reaches ζT_{\min} . Eq. (2.10-2.13) show that the ice content is affected by both w/c (assuming constant degree of hydration), temperature and RH or degree of saturation.

2.2.2 Internal pressures and ice strengthening effect

It has been widely agreed that multi pressures would initiate during the FTC process. To explain the contradictory experimental phenomenon in closed and open tests, Gong et al. (2015b) have proposed a more comprehensive internal pressure model by combining the hydraulic pressure model and the cryosuction/crystallization pressure model.

For the hydraulic pressure, both water flow theory (Powers 1949) and poro-mechanical theory of volume expansion (Coussy and Monteiro 2008) are taken into consideration. The expression of hydraulic pressure P_h is shown in Eq. (2.15). More detailed introduction could be found in Gong et al. (2015b).

$$0.09\phi\dot{\psi}_c - \frac{A}{V} \cdot \frac{m}{\eta} \cdot \frac{2}{R_E - r_E} P_h = \left(\frac{b}{K_p} + \frac{\phi\psi_c}{K_c} + \frac{\phi\psi_l}{K_l} \right) \dot{P}_h \quad (2.15)$$

where ϕ is the porosity; m is the permeability of the porous body; η is the viscosity of liquid water; K is the bulk modulus with subscripts p , c and l for porous body, ice content and liquid, respectively; b is the Biot coefficient; r_E and R_E are the equivalent radii of air void and influential radius (average spacing factor between air voids $L = 2R_E$); A and V are the equivalent empty space and influential volume; ψ represents the volume fraction in pore space with subscripts l and c standing for liquid and ice.

Due to the effect of surface tension, pressure difference exists on crystal-liquid surface and liquid-vapor surface, which result in the cryosuction pressure P_l , see **Fig. 2.3**. Assuming the pressure of vapor is same as ambient pressure (zero), the cryosuction pressure is always negative. The pressure uniformity of liquid requires that the surface tension of liquid-crystal interface is equal to that of vapor-liquid interface, which yields “ $\kappa_{CL}\gamma_{CL} = \kappa_{LV}\gamma_{LV}$ ” where κ and γ are the curvature and specific energy of interface between different phases, subscripts CL and LV stand for the liquid-crystal interface and vapor-liquid interface. Besides, it indicates that $\kappa_{CL}\gamma_{CL} = \Delta S_{fv}(T_0 - T)$ by Scherer (2005) so that cryosuction pressure can be calculated from temperature as Eq. (2.16) depending on the liquid content. Accompanied with the cryosuction pressure, the crystallization pressure P_c acts on the pore wall which depends on the shape of the pores, see **Fig. 2.3**. The formulas to calculate crystallization pressure is also given in Eq. (2.16) where ζ is the pore shape factor. As mentioned in section 2.2.1, the ice content (ψ_c) could be

affected by water cement ratio of the porous materials and temperature, thus the internal pressures would also vary with these factors. Combining the hydraulic pressure, cryosuction pressure and crystallization pressure, the effective stress σ_0 due to ice formation on porous body can be given in Eq. (2.17):

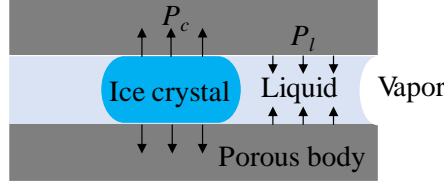


Fig. 2.3. Cryosuction and crystallization pressure in a cylindrical pore (Scherer, 2005)

$$P_l = \psi_l \cdot \Delta S_{fv} \cdot (T - T_0) \quad (2.16)$$

$$P_c = -\psi_c \cdot (1 - \zeta) \cdot \Delta S_{fv} \cdot (T - T_0)$$

$$\sigma_0 = b(p_h + p_l + p_c) \quad (2.17)$$

Besides the internal pressure by ice formation, the effective elastic properties of representative volume elements are also estimated. Based on various literatures, Gong et al. (2015b) developed a model for microscale representative volume elements composing with cement matrix, ice, liquid water and air, and upscale it to mesoscale level. The homogenized bulk (K^{hom}) and shear (G^{hom}) moduli for a general n-phase composite are calculated as:

$$\begin{cases} K^{\text{hom}} = \sum_1^n f_r K_r P_r / \sum_1^n f_r P_r \\ G^{\text{hom}} = \sum_1^n f_r G_r Q_r / \sum_1^n f_r Q_r \end{cases} \quad (2.18)$$

in which f_r is the volume fraction of phase r ; P_r and Q_r stand for the compressibility and shear compliance of phase r . The expression of compressibility and shear compliance varies on different inclusion morphology of mortar level and cement paste level where detailed information could be found in Gong et al. (2018). With given K^{hom} and G^{hom} , the effective elastic modulus and Poisson's ratio are given according to Eq. (2.19).

$$\begin{aligned}
E^{\text{hom}} &= \frac{9K^{\text{hom}}G^{\text{hom}}}{3K^{\text{hom}} + G^{\text{hom}}} \\
\nu^{\text{hom}} &= 0.5 \left(1 - \frac{1}{1/3 + K^{\text{hom}}/G^{\text{hom}}} \right)
\end{aligned} \tag{2.19}$$

2.2.3 Mesoscale constitutive relationships for springs

In mesoscopic level, for saturated concrete in non-freezing case, the normal springs of mortar, ITZ and bond behave linearly before the stress reaches the tensile strength f_t . Once the tensile strain exceeds the threshold value ε_0 , the stress will decrease linearly with increasing strain, see the black lines in **Fig. 2.4**. If freezing temperature is obtained and ice forms, enhanced elastic properties are taken into consideration for mortar, ITZ and bond. As a result, the elastic modulus of normal springs of mortar, ITZ and bond interface would increase from k_n to k_n' . In other words, the constitutive curves of these springs would shift from the black lines to the red lines under freezing temperature (see **Fig. 2.4**). Besides, it should be emphasized that no ice is assumed to take place in aggregate, thus the elastic modulus of normal springs of aggregate are not enhanced during the freezing temperature.

To consider the influence by frost damage, the linear unloading-reloading path developed by Ueda et al. (2009) is adopted after the maximum historical strain reaches ε_0 , see the solid black curves in **Fig. 2.4** and **2.5**. The envelope curve will point to a compressive strain ε_{pa} , which could be calculated based on experimental data. It should be noted that two systems exist in the frozen cementitious material: the porous body system and ice-liquid system. The effective internal pressure due to ice formation $\sigma_0 = b(P_h + P_l + P_c)$ takes place firstly in the ice-liquid system. With expansion of the porous body, this effective pressure σ_0 is released until an equilibrium is achieved between two systems, referring to the intersection point in **Fig. 2.4**. For convenience of the simulation, the internal pressure σ_0 is applied externally on both systems instead of internally on the ice-liquid system as long as the final stress (σ_p) and strain (ε_{ta}) of porous body are same, as shown in **Fig. 2.5**.

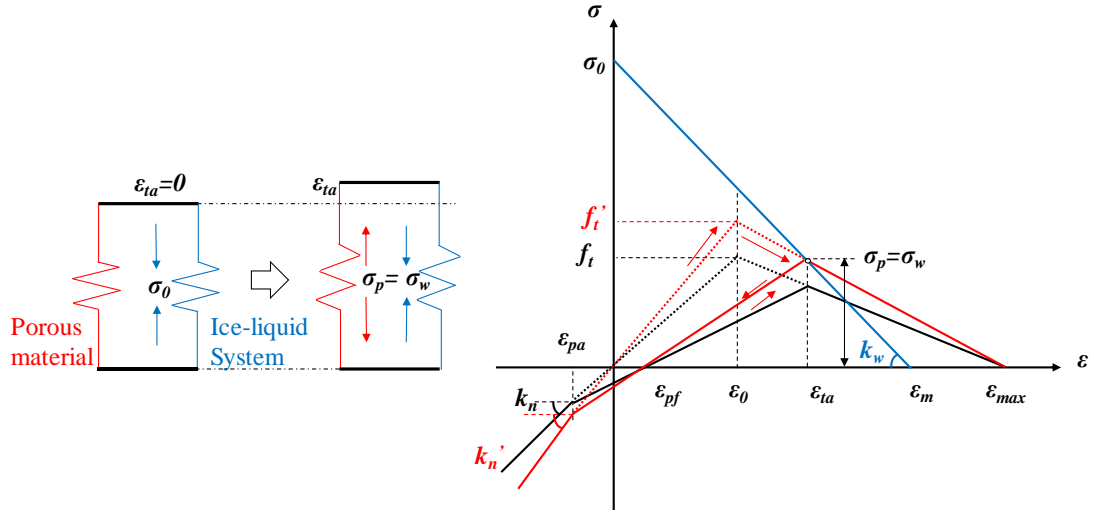


Fig. 2.4. Mesoscale stress-strain of normal spring (σ_0 added internally, Gong et al. 2018)

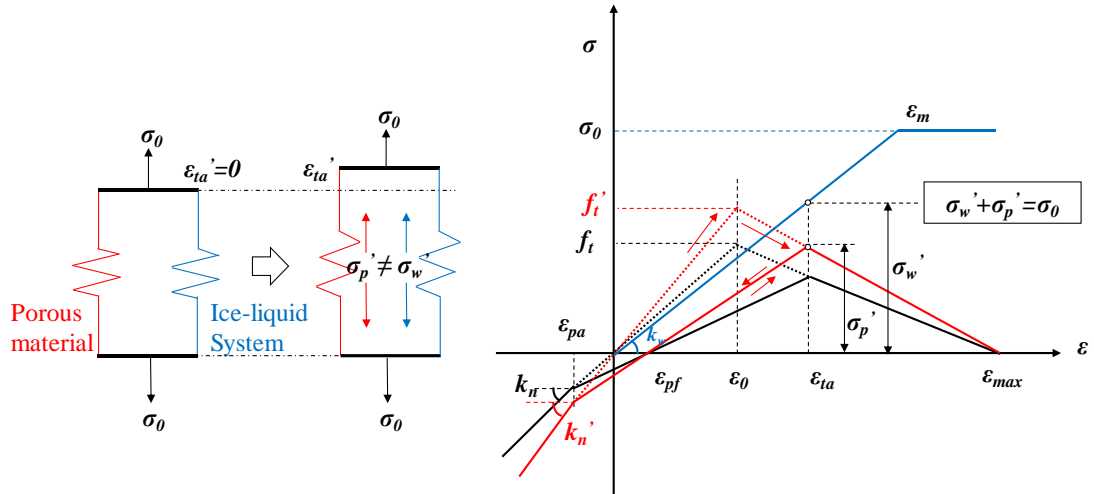


Fig. 2.5. Mesoscale stress-strain of normal spring (σ_0 added externally, Gong et al. 2018)

References

- T. Kawai, New discrete models and their application to seismic response analysis of structures, *Nuclear Engineering and Design*. 48 (1) (1978) 207-229.
- J.E. Bolander Jr, S. Saito, Fracture analyses using spring networks with random geometry, *Engineering Fracture Mechanics*. 61 (5-6) (1998) 569-591.
- S. Muto, H. Nakamura, T. Tanabe, W. Srisoros, S. Lee, Analysis of bond characteristics between concrete and deformed bar by meso-scale analysis, *Journal of Applied Mechanics*. 7 (2004) 767-774.
- K. Nagai, Y. Sato, T. Ueda, Mesoscopic simulation of failure of mortar and concrete by 2D RBSM, *Journal of Advanced Concrete Technology*. 2 (3) (2004) 359-374.
- K. Nagai, Y. Sato, T. Ueda, Mesoscopic simulation of failure of mortar and concrete by 3D RBSM, *Journal of Advanced Concrete Technology*. 3 (3) (2005) 385-402.
- H. Nakamura, W. Srisoros, R. Yashiro, M. Kunieda, Time-dependent structural analysis considering mass transfer to evaluate deterioration process of RC structures, *Journal of Advanced Concrete Technology*. 4 (1) (2006) 147-158.
- L. Wang, T. Ueda, Mesoscale modeling of water penetration into concrete by capillary absorption, *Ocean Engineering*. 38 (2011) 519-528.
- D. Hayashi, K. Nagai, L. Eddy, Mesoscale analysis of RC anchorage performance in multidirectional reinforcement using a three-dimensional discrete model, *Journal of Structural Engineering*, 143 (7) (2017) 04017059.
- T. Ueda, M. Hasan, K. Nagai, Y. Sato, L. Wang, Mesoscale simulation of influence of frost damage on mechanical properties of concrete, *Journal of Materials in Civil Engineering*. 21 (6) (2009) 244-252.
- F. Gong, Y. Wang, D. Zhang, T. Ueda, Mesoscale simulation of deformation for mortar and concrete under cyclic freezing and thawing stress, *Journal of Advanced Concrete Technology*. 13 (6) (2015a) 291-304.
- F. Gong, T. Ueda, Y. Wang, D. Zhang, Z. Wang, Mesoscale simulation of fatigue behavior of concrete materials damaged by freeze-thaw cycles, *Construction and Building Materials*. 144 (2017) 702-716.

- G.W. Scherer, J. Valenza, Mechanisms of frost damage, *Materials Science of Concrete*. 7 (60) (2005) 209-246.
- Y. Xi, Z.P. Bazant, H.M. Jennings, Moisture diffusion in cementitious materials Adsorption isotherms, *Advanced Cement Based Materials*. 1 (6) (1994) 248-257.
- F. Gong, E. Sicat, D. Zhang, T. Ueda, Stress analysis for concrete materials under multiple freeze-thaw cycles, *Journal of Advanced Concrete Technology*. 13 (3) (2015b) 124-134.
- Z. Sun, G. W. Scherer, Effect of air voids on salt scaling and internal freezing temperatures, *Cement and Concrete Research*. 40 (2) (2010) 260-270.
- T. C. Powers, The air requirement of frost-resistance of concrete, *Proceedings of Highway Research Board*. 29 (1949) 184-211.
- O. Coussy, P.J. Monteiro, Poroelastic model for concrete exposed to freezing temperatures, *Cement and Concrete Research*. 38 (1) (2008) 40-48.
- F. Gong, T. Ueda, D. Zhang, Two-dimensional rigid body spring method based micro-mesoscale study of mechanical strengthening/damaging effects to concrete by frost damage, *Structural Concrete*. 19 (4) (2018) 1131-1145.

Chapter 3

3. Meso-macro Simulation and Modeling of Concrete

3.1 Simulation Models

Meso-macro simulations were conducted to model the deteriorated material behaviors of concrete under the effect of frost damage. 100x200 mm² concrete specimen with 40% volume fraction of coarse aggregates randomly sprayed inside the model. Grain size distribution was given on basis of JSCE standard. Around 2600 meshes were divided for each model where the dimension was approximately 3 mm.

According to Eq. (2.9), the material inputs were calculated and applied into the program. The values of elastic modulus of aggregate E_a , Poisson's ratio of mortar ν_m , Poisson's ratio of aggregate ν_a were set to be constant values of 50 GPa, 0.18 and 0.25 while the frictional angle in shear criterion of ITZ (in Eq. (2.6)) was set a typical value of 35° (Nagai et al. 2004). Fully saturated was assumed for all models and the porosity could be calculated by water cement ratio following the procedures below:

The normalized water content by weight of cement paste W_{sat} was given in Eq. (3.1), the total volume ratio of pores in cement paste ϕ_{cp} and mortar ϕ_m (neglecting the pore volume in ITZ) would be (Gong et al. 2017):

$$\phi_{cp} = \frac{W_{sat} / \rho_{wat}}{1 / \rho_{solid} + W_{sat} / \rho_{wat}} \quad (3.1)$$
$$\phi_m = f_{cp} \cdot \phi_{cp}$$

where f_{cp} was the volume fraction of cement paste in mortar which could be determined by:

$$f_{cp} = 1 - f_{sand} = 1 - \frac{m_{sand} / \rho_{sand}}{m_{sand} / \rho_{sand} + m_{wat} / \rho_{wat} + m_{cem} / \rho_{cem}} \quad (3.2)$$

Here a linear relationship between f_{cp} and w/c was proposed depending on Sicat et al. (2014)'s experiment where $f_{cp} = 0.313w/c + 0.486$. All the necessary material inputs could be given according to Eq. (2.9), (3.1) and (3.2). The effect that non-uniform porosity and thickness of ITZ due to bleeding and gravity might affect the frost damage was neglected since the thickness of ITZ was assumed to be zero in the Rigid Body Spring Model for simplicity.

As mentioned above, the water cement ratio (w/c), minimum temperature of each FTC (T_{min})

and the numbers of FTC (N) were chosen to be the variables. Three types of concrete model were prepared depending on water cement ratio (0.4, 0.5 and 0.6) for consideration of the common adopted cases in both laboratory tests and engineering applications. The material inputs for concrete models were calculated based on Eq. (2.9), (3.1) and (3.2) and they were listed in **Table 3.1**.

Table 3.1. Material inputs for concrete models with different w/c

w/c	f_{cm}' (MPa)	E_m (MPa)	f_{tp} (MPa)	f_{ti} (MPa)	c_i (MPa)	ϕ_m
0.4	42.55	23380.81	3.75	1.72	2.86	0.179
0.5	31.91	21165.66	3.35	1.58	2.60	0.217
0.6	24.82	19230.54	3.00	1.44	2.34	0.257

For each RBSM model (with certain water cement ratio), firstly an entire process of FTC (with specific minimum temperature T_{\min} and number of cycles N) was applied. For each type of model, five cases of FTC were adopted depending on different minimum temperature of each cycle (-10, -15, -20, -30 and -40 °C) and the numbers of FTC (50, 100, 150, 200 and 300 cycles), respectively. Additionally, a reference model without frost damage was simulated for comparison. Afterwards, the behaviors of frost-damaged model under mechanical external loading including uniaxial compression and tension was simulated. With the simulation results, parametric studies were executed.

It should be noted that in this simulation, no temperature and moisture gradients were assumed, which in other words, the heat and moisture field was uniform inside the model. Thus, the damage took place uniformly in spite of the positions. Besides, the fact that no obvious difference whether the temperature changing rate were considered pertaining to the final status of frost-damaged concrete had been indicated in previous works. In order to achieve faster computation speed, simplification was adopted where temperature changing rate was neglected. After FTC finished, the models were applied with uniaxial compressive and tensile loads by actuating prescribed displacement load on top surface of the model while the bottom surface was restrained in vertical direction. Loading rate for uniaxial compression and tension were set differently to be 0.005 mm/step and 0.001 mm/step respectively. For other boundary conditions, horizontal and rotational restraints were given to both loading and supporting surfaces.

3.2 Simulation Results

3.2.1 Residual strain and meso-cracks after FTC

Unrecoverable plastic tensile deformation was induced owing to the meso-cracks initiated by frost damage, which was also observed in many previous experiments. **Fig. 3.1** showed the vertical strain of C0.5-20 model suffering 300 freezing-thawing cycles and the meso-cracks illustration at the end of 200th cycle. In **Fig. 3.1**, the short red lines meant that the crack width had reached 0.005 mm in normal springs. Since ITZ usually acted as the weakest part in concrete, meso-cracks would initiate in the ITZ part earlier than in the mortar part, which could also be seen in **Fig. 3.1**. The simulated values of residual tensile strain were listed in **Table 3.2** for two reasons: 1. The residual plastic strain was able to be measured experimentally, which could be treated as the damage index; 2. Almost no material test with concrete suffering frost damage could be found to report such information.

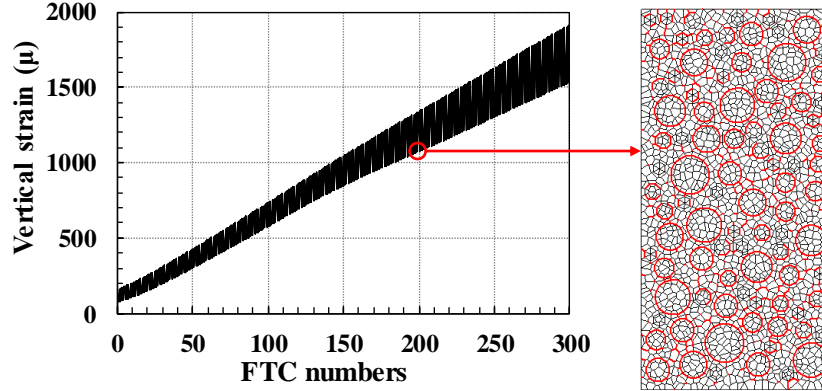


Fig. 3.1. Vertical strain during 300 FTCs and meso-crack propagation (0.005mm)

Table 3.2. Residual tensile strain for all the models (μ)

Model	w/c	T_{\min} (°C)	FTC Numbers				
			50	100	150	200	300
C0.4-10	0.4	-10	0.01	0.12	10.39	77.85	390.77
C0.4-15		-15	7.48	68.03	203.61	380.09	741.28
C0.4-20		-20	108.30	273.95	455.48	638.06	976.03
C0.4-30		-30	353.31	536.77	729.90	891.98	1208.73
C0.4-40		-40	430.76	621.81	793.96	954.33	1264.24

C0.5-10		-10	0	10.59	132.01	388.44	932.22
C0.5-15		-15	56.54	265.34	540.19	813.71	1290.58
C0.5-20	0.5	-20	305.12	578.84	847.09	1083.16	1528.94
C0.5-30		-30	621.61	892.29	1106.80	1354.76	1795.19
C0.5-40		-40	725.30	970.76	1186.92	1421.88	1865.34
C0.6-10		-10	0.21	92.62	440.41	828.19	1470.63
C0.6-15		-15	183.01	560.34	921.58	1200.44	1872.15
C0.6-20	0.6	-20	533.18	904.39	1231.07	1545.35	2174.17
C0.6-30		-30	903.83	1223.22	1527.38	1843.16	2229.35
C0.6-40		-40	985.54	1308.04	1608.42	/	/

3.2.2 Degradation of compressive behaviors

The compressive strength for both intact and damaged concrete were listed in **Table 3.3** where it could be indicated the compressive strength of concrete diminished obviously with increasing numbers of FTC, lower temperature cycles and larger water cement ratio. Similar tendency was also found in various experimental results, see Table 1.1. As an instance, **Fig. 3.2** showed the compressive stress-strain relationship of C0.5-20 specimens after suffering different numbers of FTC. In addition, the cracking failure patterns and deformation at post peak stage of the intact specimen were also plotted. In **Fig. 3.2**, the short red lines meant that crack reached maximum value (the strains of normal springs had reached ε_{\max}) which made the normal springs ineffective to sustain any load (see **Fig. 2.4** and **2.5**). It should be mentioned that the deformation in **Fig. 3.2** had been enlarged by 10 times. From **Fig. 3.2**, it could be seen that the compressive strength (f_c) would decrease with accumulation of frost damage while the compressive strain at peak stress (ε_c) would show continuous increase. Moreover, the stiffness of frost-damaged concrete showed obvious diminishment with “stiffness recovery” effect: the stiffness of frost-damaged concrete had a reduced value at first owing to the meso-cracks induced by frost action but later recovered to a higher value along with the closure of cracks. This phenomenon was also observed and explained by several experimental works, e.g. Hasan et al. (2004), Zou et al. (2008), Duan et al. (2011) and Cao et al. (2013) etc.

Table 3.3. Compressive strength for all the models (MPa)

Model	w/c	T_{min} (°C)	FTC Numbers					
			0	50	100	150	200	300
C0.4-10	0.4	-10		29.93	29.83	28.94	30.14	27.39
C0.4-15		-15		31.22	32.01	27.87	30.43	25.52
C0.4-20		-20	30.88	30.11	30.36	25.80	24.29	19.97
C0.4-30		-30		27.78	24.09	23.49	19.71	15.51
C0.4-40		-40		27.00	24.65	21.64	19.07	15.52
C0.5-10	0.5	-10		25.49	23.00	24.40	22.09	13.78
C0.5-15		-15		26.21	23.52	20.01	14.69	11.21
C0.5-20		-20	24.98	23.89	20.57	16.44	12.01	8.99
C0.5-30		-30		20.73	14.36	12.75	10.45	7.23
C0.5-40		-40		20.49	13.13	12.86	10.26	6.58
C0.6-10	0.6	-10		20.00	18.72	17.94	14.28	7.51
C0.6-15		-15		18.85	16.05	10.40	11.98	5.34
C0.6-20		-20	21.20	16.39	12.13	9.97	7.31	4.34
C0.6-30		-30		12.15	8.3	7.16	5.71	4.43
C0.6-40		-40		10.71	7.80	7.15	/	/

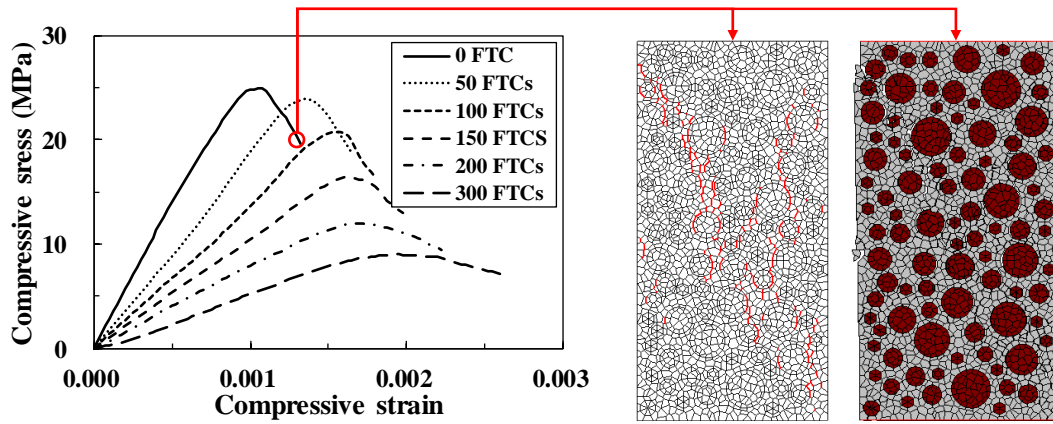


Fig. 3.2. Stress-strain relationship for C0.5-20 series, crack pattern and deformation

To model the deterioration of compressive strength for frost-damaged concrete, Berto et al. (2015) suggested to use an environmental damage parameter d_{env} ($=1-f_{cd}/f_c$) where f_c and f_{cd} represented the compressive strength of intact and frost-damaged concrete, see Eq. (3.3). The environmental damage parameter d_{env} could be calculated based on Eq. (3.4) when the ASTM C666-A frost damage condition was adopted (Berto et al. 2014, 2015). In Eq. (3.4), λ was a parameter depending on the compressive strength of intact concrete f_c ; N_{eq} was called the

equivalent number of FTCs on basis of ASTM C666-A condition which could be calculated depending on the actual number of FTC (N), as shown in Eq. (3.5):

$$d_{env} = 1 - \frac{f_{cd}}{f_c} \quad (3.3)$$

$$d_{env} = \lambda N_{eq} \quad (3.4)$$

$$N_{eq} = \chi N^\beta \quad (3.5)$$

in which χ and β were parameters depending on experimental conditions. Substituting Eq. (3.3) and (3.5) into Eq. (3.4) and letting $\alpha = \chi \cdot \lambda$, the relative compressive strength $Rf_c (=f_{cd}/f_c)$ would be expressed as Eq. (3.6) where α and β were parameters relating to concrete strength (w/c) and FTC conditions (w/c , T_{min}). Through fitting the simulation results with Eq. (3.6), it was found that compressive strength was approximately linear-proportional to the numbers of FTC. Thus, β could be adopted with 1.0. Meanwhile, α could be determined by water cement ratio w/c and minimum temperature T_{min} , as shown in Eq. (3.7):

$$Rf_c = 1 - \alpha N^\beta \quad (3.6)$$

$$\alpha = \left[\left(1.5 \frac{w}{c} + 0.6 \right) \cdot \ln(-T_{min}) + \left(6 \frac{w}{c} - 5.1 \right) \right] \times 10^{-3} \quad (3.7)$$

$$\beta = 1.0$$

Eq. (3.6) and (3.7) were the proposed prediction model to calculate the compressive strength of frost-damaged concrete with given conditions, including water cement ratio, temperature of FTC and numbers of FTC. Relative compressive strength Rf_c was adopted in this model in order to eliminate the effect from different morphologies of the specimens. To verify the reliability of the model, various available experimental results were used to demonstrate the predicted compressive strengths of frost-damaged concrete, which was calculated by Eq. (3.6) and (3.7). As shown in **Fig. 3.3**, satisfactory agreement was found between test and analytical results, which strongly proved the applicability of the proposed model.

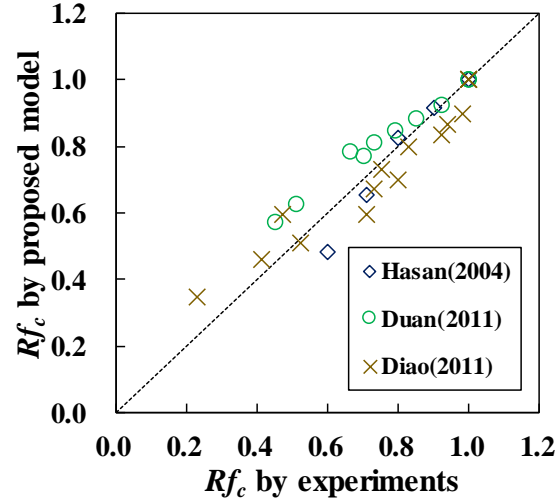


Fig. 3.3. Comparison of Rf_c by proposed model and experiments

The elastic modulus (E_{cd}) and compressive strain at peak stress (ε_{cd}) of frost-damaged concrete were also important factors when evaluating the compressive behaviors. Several literatures had suggested that the damaged elastic modulus and compressive strain at peak stress could be related to the relative compressive strength Rf_c . Thus, the simulated values of relative elastic modulus RE_c ($=E_{cd}/E_c$) and relative compressive strain at peak stress $R\varepsilon_c$ ($=\varepsilon_{cd}/\varepsilon_c$) were plotted versus the relative compressive strength Rf_c in **Fig. 3.4 and 3.5**. Meanwhile, empirical formulas were developed with data-fitting so that the value of RE_c and $R\varepsilon_c$ could be calculated based on the relative compressive strength Rf_c , as shown in Eq. (3.8). **Fig. 3.6 and 3.7** showed the comparison between Eq. (3.8) and available experimental data by various scholars, where good correlations were found for both RE_c and $R\varepsilon_c$, which further verified the reliability of the simulation results as well as the proposed models.

$$\begin{aligned} RE_c &= 1.284^{2.932 \cdot Rf_c} - 1.081 \\ R\varepsilon_c &= -1.261Rf_c + 2.261 \end{aligned} \tag{3.8}$$

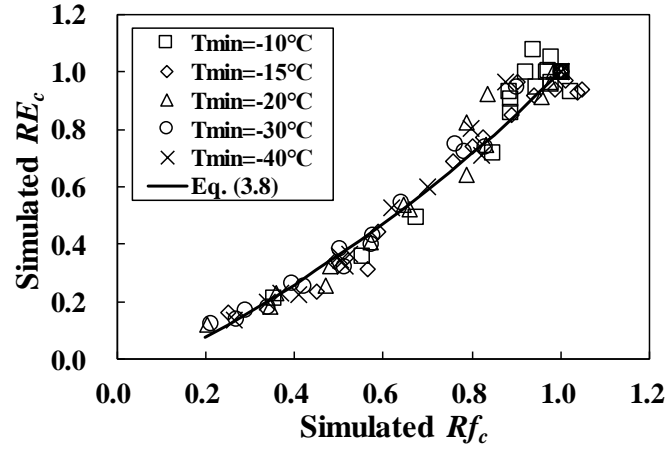


Fig. 3.4. Relationships between RE_c versus Rf_c by RBSM simulation

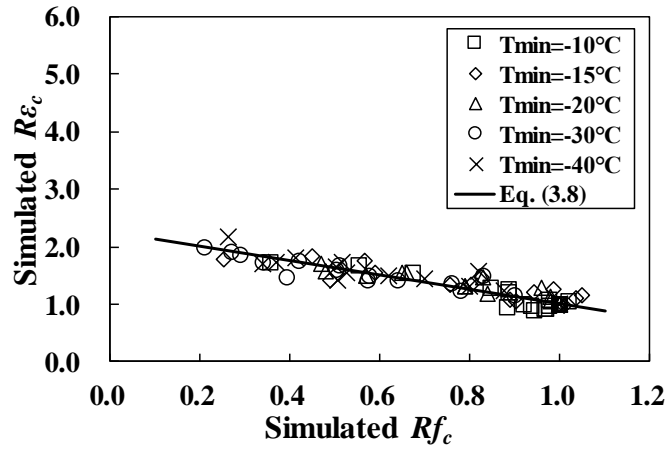


Fig. 3.5. Relationships between RE_c versus Rf_c by RBSM simulation

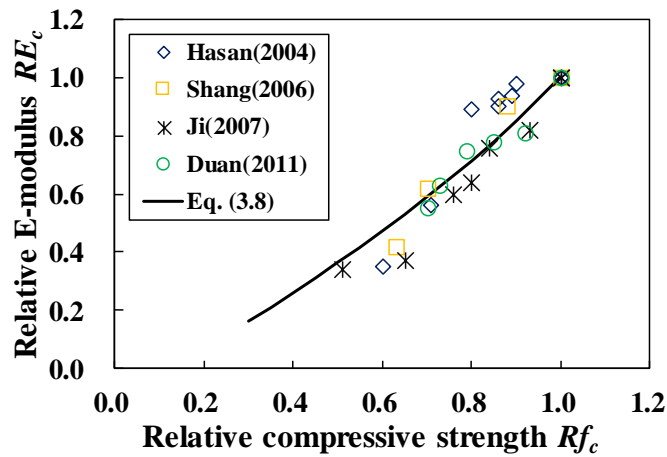


Fig. 3.6. Comparisons of RE_c between proposed models and experiments

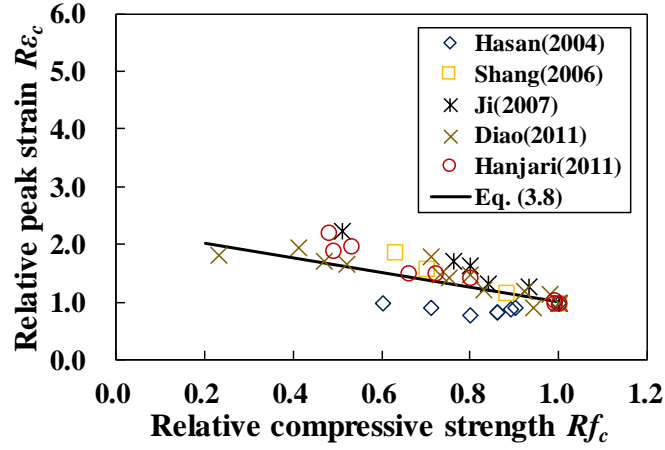


Fig. 3.7. Comparisons of $R\epsilon_c$ between proposed models and experiments

3.2.3 Degradation of tensile behaviors

Besides the compressive behaviors, the tensile strength of frost-damaged concrete was also analyzed and modeled with the meso-macro simulation results by 2D mesoscale RBSM. **Fig. 3.8** showed an example of tensile stress-strain curves of C0.5-20 specimens after suffering different numbers of FTC, together with the cracking failure pattern and deformation at post peak of intact concrete. In **Fig. 3.8**, the short red lines meant that the strains of normal springs had reached ϵ_{\max} which made the normal springs ineffective (see **Fig. 2.4** and **2.5**) and the deformation had been enlarged by 50 times. Again, since ITZ acted as the weakest part of concrete, the failure pattern happened along ITZ as much as possible.

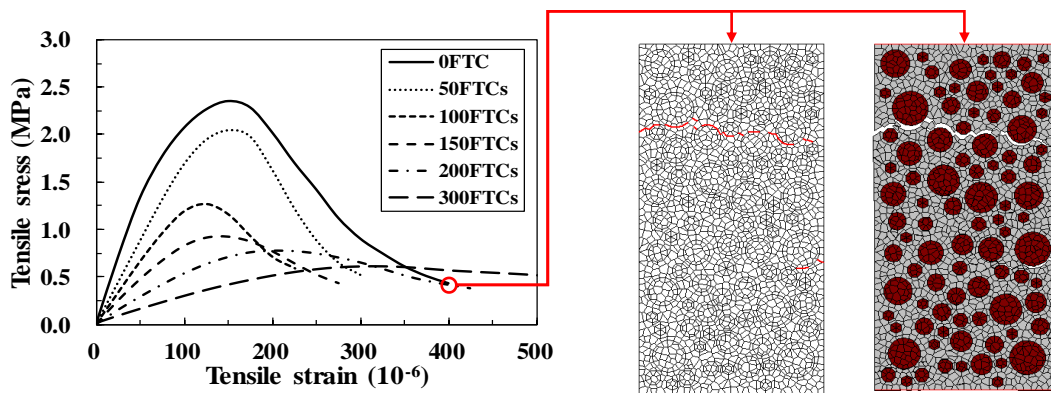


Fig. 3.8. Stress-strain relationships for C0.5-20 series, crack pattern and deformation

The relationship between compressive strength and tensile strength had already been established for intact concrete by several standards, e.g. fib Model Code 2010, Euro Code 2, etc. For frost-damaged concrete, such relationship was still in lacking. However, some studies reported to calculate the deteriorated tensile strength on basis of the damaged compressive strength. They had proposed empirical models with their own experimental results. Following this way, the meso-macro simulation results between compressive and tensile strength of frost-damaged concrete were plotted in **Fig. 3.9**. It could be found the tensile strength always had a higher reduction than the compressive strength, which was observed in many previous studies as well. Through fitting the simulation data in **Fig. 3.9**, the model to calculate relative tensile strength Rf_t was proposed in Eq. (3.9). Comparison was made between the analytical and experimental results, in which good agreement could be achieved as shown in **Fig. 3.10**.

$$Rf_t = 0.89e^{3.13 \cdot (Rf_c - 1)} + 0.11 \quad (3.9)$$

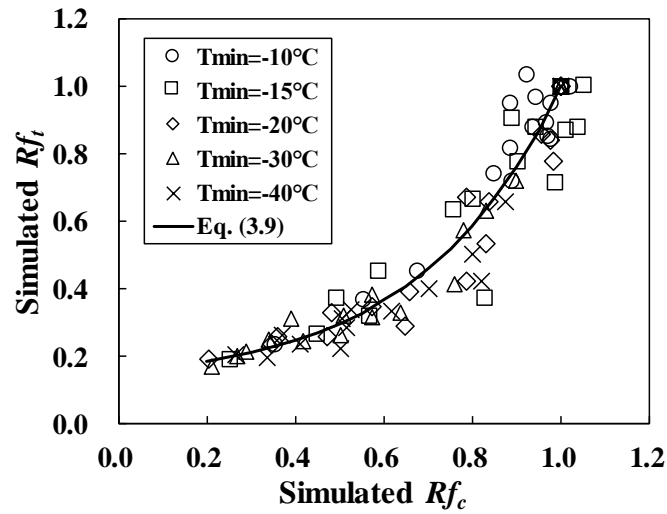


Fig. 3.9. Relationships between Rf_t versus Rf_c by RBSM simulation

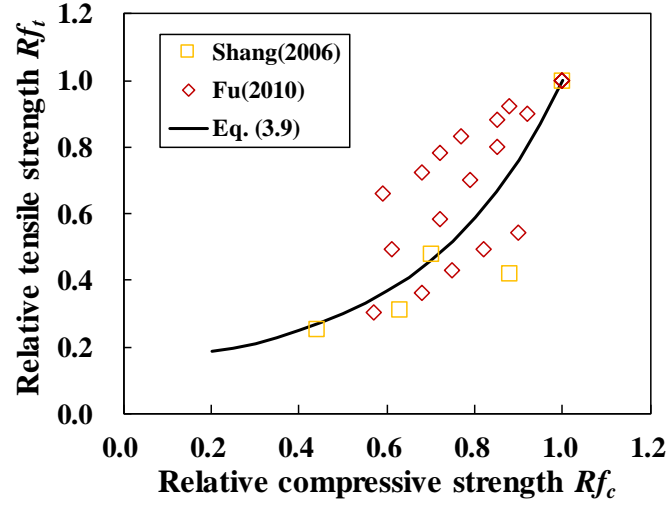


Fig. 3.10. Comparison of Rf_t between proposed model and experiments

3.3 Modeling of Deteriorated Constitutive Relationships

3.3.1 Compressive stress-strain curve

Many mathematical equations could be found to express the compressive stress-strain relationship of intact concrete. As stated in section 3.2.2, the pre-peak compressive behaviors of frost-damaged concrete had an obvious stiffness change, which was attributed to the randomly-oriented cracks in concrete induced by frost damage before mechanical external loading. Thus, the compressive load would actuate on concrete with lower stiffness before the closure of cracks, and then concrete showed a stiffer (still lower than the sound value) pre-peak behavior. To consider such phenomena, a stress-strain relationship originally developed by Guo et al. (2003) was adopted to model the complete compressive constitutive relationship for frost-damaged concrete. Since the model had two shape controlling factors, which could express such “stiffness recovery”, as shown in Eq. (3.10):

$$y = \begin{cases} ax + (3 - 2a)x^2 + (a - 2)x^3, & 0 \leq x \leq 1 \\ \frac{x}{b(x-1)^2 + x}, & x \geq 1 \end{cases} \quad (3.10)$$

where $y = \sigma/f_{cd}$ and $x = \varepsilon/\varepsilon_{cd}$; σ and ε represented the compressive stress and strain; a and b were independent parameters to control the shape of the pre-peak and post-peak curves, which could be adopted as the suggestions by Guo et al. (2003). To calculate the parameters a_d and b_d for

frost-damaged concrete, Duan et al. (2011) suggested using the damaged compressive strength as index while Zou et al. (2008) and Cao et al. (2013) suggested adopting relative dynamic elastic modulus. For convenience, here the relative compressive strength was utilized to calculate the parameters a_d and b_d .

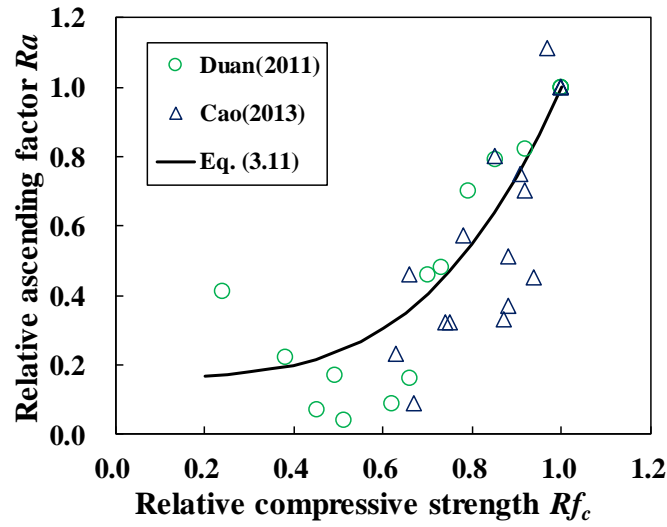


Fig. 3.11. Relationships between relative compressive strength and Ra

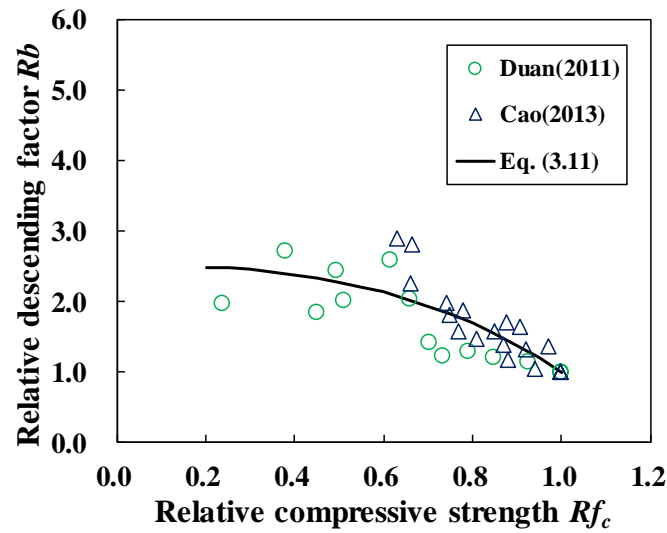


Fig. 3.12. Relationships between relative compressive strength and Rb

In **Fig. 3.11** and **3.12**, the regression models to calculate the normalized ascending/descending shape controlling factors Ra ($=a_d/a$) and Rb ($=b_d/b$) were plotted among the test results by Duan et al. (2011) and Cao et al. (2013). Formulas of the models were given as Eq. (3.11).

$$\begin{aligned}
Ra &= 0.167 + 0.833(Rf_c)^{3.512} \\
Rb &= 2.507 - 1.507(Rf_c)^{2.715}
\end{aligned}
\tag{3.11}$$

Eq. (3.10) was the compressive stress-strain relationship, which was developed on basis of the RBSM simulation results and experimental data. To explain more clearly, the procedure to derive the compressive constitutive relationship of frost-damaged concrete follows: Firstly, calculate the damaged compressive strength and strain at peak compressive stress according to Eq. (3.6) and (3.8); Secondly, calculate the shape controlling parameters referring to Eq. (3.11); Finally, substitute all the results into Eq. (3.10) and achieve the complete compressive stress-strain relationship for frost-damaged concrete. In order to demonstrate the proposed constitutive relationship, experimental results by Hanjari et al. (2011) was compared with the analytical results, see Fig. 3.13. In Fig. 3.13, “EXP.” and “CAL.” represented for the experimental and calculated results where satisfactory agreements could be found.

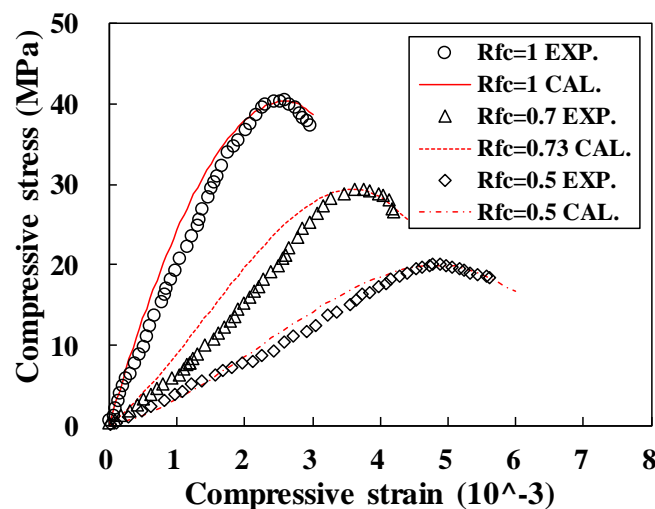


Fig. 3.13. Experimental and analytical compressive stress-strain curves

3.3.2 Tensile stress-strain curve

The crack was defined to start propagation when tensile stress had reached the tensile strength. Thus, the complete tensile stress-strain curve was divided into two parts: for pre-peak branch where tensile stress had not reached the tensile strength yet, linear behavior was adopted where the frost-damaged tensile strength and stiffness (same as the elastic modulus for

compression) could be calculated according to Eq. (3.9) and (3.8); for post-peak branch where tensile stress had reached the tensile strength and crack initiated, a simplified bi-linear relationship was proposed in the model based on test results by Hanjari et al. (2011), which could be easily utilized in the FEM application. To further describe it: if drawing the relationship of σ_t/f_{td} versus $w/w_{d\max}$ curve, the inflection point of post-peak bi-linear curve would always pass (0.14, 0.17), see Eq. (3.12). In which, σ_t and ε_t were tensile stress and strain; ε_{td} could be calculated as f_{td}/E_{cd} ; w and $w_{d\max}$ stood for the crack width and maximum crack width for frost-damaged concrete where $w_{d\max}$ could be calculated by fitting Hasan et al. (2002)'s and Hanjari et al. (2011)'s experimental data in spite of large scattering, see Eq. (3.13) and **Fig. 3.14**. w_{\max} was the maximum crack width which could be measure in the laboratory test (0.8 mm and 0.2 mm for Hasan et al. 2002 and Hanjari et al. 2011). The analytical post-peak model was also illustrated together with Hasan et al.'s (2002) tested results, see **Fig. 3.15**. It could be indicated that the tension-softening curve proposed in Eq. (3.12) had a good correlation with the experimental results.

$$\sigma_t = E_{cd} \cdot \varepsilon_t, \varepsilon_t \leq \varepsilon_{td}$$

$$\frac{\sigma_t}{f_{td}} = 1 - 5.929 \frac{w}{w_{d\max}}, \varepsilon_t \geq \varepsilon_{td} \ \& \ \frac{w}{w_{d\max}} \leq 0.14 \quad (3.12)$$

$$\frac{\sigma_t}{f_{td}} = 0.198 \left(1 - \frac{w}{w_{d\max}} \right), \varepsilon_t \geq \varepsilon_{td} \ \& \ \frac{w}{w_{d\max}} > 0.14$$

$$w_{d\max} = w_{\max} \times 6.716e^{-1.821Rf_t} \quad (3.13)$$

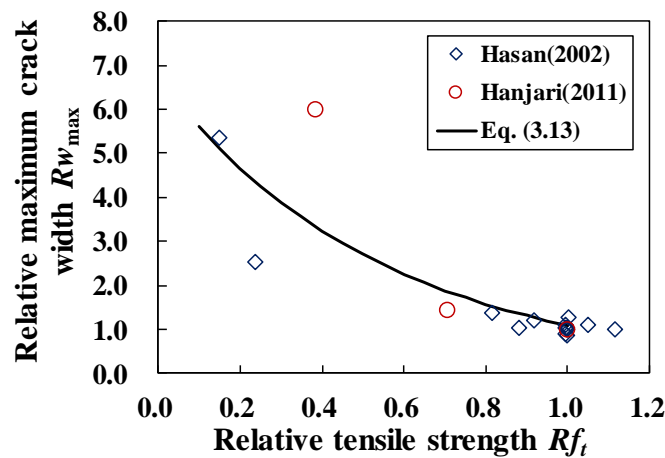


Fig. 3.14. Relationships between relative tensile strength and $Rw_{d\max}$

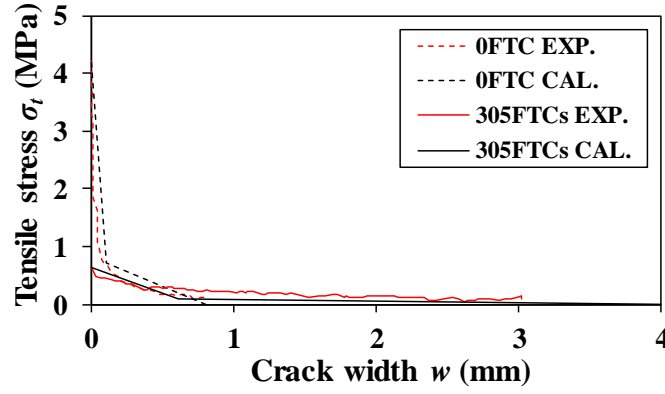


Fig. 3.15. Comparison between experimental and analytical tension softening curves

3.4 Conclusions of This Chapter

Following conclusions could be drawn from current chapter:

- (1) 2D mesoscale Rigid Body Spring Model was adopted to evaluate and model the compressive and tensile behaviors of concrete under the effect of frost damage. Similarly like observed in many previous experiments, the simulation results showed that the frost action had significant influence on the mechanical behaviors of concrete.
- (2) According to the simulation results, the model to predict the compressive strength of frost-damaged concrete was proposed, which comprised various cases with different water cement ratio, minimum temperature and number of freezing thawing cycles. Using normalized compressive strength as the damage index, other deteriorated material properties such as tensile strength, elastic modulus and compressive strain at peak stress were also empirically modeled on basis of the meso-macro simulation results. The analytical results had satisfactory correlations with experimental data which strongly demonstrated the reliability and applicability of the models.
- (3) Constitutive laws including compressive and tensile stress-strain relationships of frost-damaged concrete were proposed based on several experimental results, which can be further applied to the structural analysis of frost-damaged RC structures with Finite Element Method.

References

- Japan Society of Civil Engineers, Standard specification for concrete structures, Tokyo: JSCE. (2007).
- K. Nagai, Y. Sato, T. Ueda, Mesoscopic simulation of failure of mortar and concrete by 2D RBSM, *Journal of Advanced Concrete Technology*. 2 (3) (2004) 359-374.
- F. Gong, Y. Wang, T. Ueda, D. Zhang, Modeling and mesoscale simulation of ice-strengthened mechanical properties of concrete at low temperatures, *Journal of Engineering Mechanics*. 143 (6) (2017) 04017022.
- E. Sicat, F. Gong, T. Ueda, D. Zhang, Experimental investigation of the deformational behavior of the interfacial transition zone (ITZ) in concrete during freezing and thawing cycles, *Construction and Building Materials*. 65 (2014) 122-131.
- M. Hasan, H. Okuyama, H. Sato, T. Ueda, Stress-strain model of concrete damaged by freezing and thawing cycles, *Journal of Advanced Concrete Technology*. 2 (1) (2004) 89-99.
- C. Zou, J. Zhao, F. Liang, Stress-strain relationship of concrete in freeze-thaw environment, *Frontiers of Architecture and Civil Engineering in China*. 2 (2) (2008) 184-188.
- A. Duan, W. Jin, J. Qian, Effect of freeze-thaw cycles on the stress-strain curves of unconfined and confined concrete, *Materials and Structures*. 44 (7) (2011) 1309-1324.
- D. Cao, L. Fu, Z. Yang, X. Qin, Study of constitutive relations of compresses concrete subjected to action of freezing-thawing cycles, *Journal of Building Materials*. 16 (1) (2013) 17-23.
- L. Berto, A. Saetta, D. Talledo, Constitutive model of concrete damaged by freeze-thaw action for evaluation of structure performance of RC elements, *Construction and Building Materials*. 98 (2015) 559-569.
- L. Berto, A. Saetta, D. Talledo, R. Vitaliani, Structural analysis of frost damaged constructions of a coupled environmental-mechanical damage model, *Proceedings of the Joint 11th World Congress on Computational Mechanics*. Barcelona (2014) 904-915.
- American Society for Testing and Materials Committee, Standard test method for resistance of concrete to rapid freezing and thawing (ASTM C666-03), West Conshohocken: ASTM International. (2003).
- H. Shang, Y. Song, Experimental study of strength and deformation of plain concrete under

biaxial compression after freezing and thawing cycles, *Cement and Concrete Research*. 36 (10) (2006) 1857-1864.

X. Ji, The experimental study and theoretical analysis on the mechanical performance of concrete and bond behavior between concrete and steel bar after freezing and thawing, Doctoral Dissertation. Dalian University of Technology (2007).

International Federation for Structural Concrete, Fib model code for concrete structures 2010, Berlin: Ernst & Sohn. (2013).

British Standards Institution, Eurocode 2: Design of concrete structures: British standard, London: BSi. (2008).

L. Fu, Experimental study on the strength of concrete under uniaxial tensile load after freeze-thaw cycles, Master Dissertation. Yangzhou University (2010).

Z. Guo, X. Shi, Reinforced concrete theory and analysis. Tsinghua University Press (2003).

K.Z. Hanjari, P. Utgenannt, K. Lundgren, Experimental study of the material and bond properties of frost-damaged concrete, *Cement and Concrete Research*. 41(3) (2011) 244-254.

M. Hasan, K. Nagai, Y. Sato, T. Ueda, Tensile stress-crack model for plain concrete damaged by freezing and thawing action, *Proceedings of Japan Concrete Institute*. 24 (2) (2002) 109-114.

Chapter 4

4. Meso-macro Simulation and Modeling of Bond

4.1 Axisymmetric Mesoscale RBSM

4.1.1 Basic concepts

Axisymmetric model can be categorized into the two-dimensional analytical methods. However, different from the 2D plane stress/strain methods, axisymmetric model can evaluate the out-of-plane stress and strain components as well (Kambayashi et al. 1999, Yao et al. 1995, etc.). In the polar coordinate system, circumferential strain and stress of the element will initiate once deformation takes place in the radial direction, see **Fig. 4.1**.

Similarly like the 2D mesoscale RBSM described in chapter 2 and 3, the axisymmetric mesoscale RBSM model is also divided into polyhedron elements with random mesh using Voronoi diagram where the elements are connected by springs. Each Voronoi cell represents a mortar, aggregate or reinforcement element with two translational and one rotational degree of freedom locating at the center of gravity of the element. For two connecting elements, there are three springs linking them, i.e. normal spring, shear spring and circumferential spring, which are placed at the midpoint of boundary between two elements (see **Fig. 4.1**). Following the suggestion by Takeuchi et al. (1980), the stiffness values of springs Ksp are calculated according to Eq. (4.1) where subscripts n , φ and s stand for normal spring, circumferential spring and shear spring, respectively. E_{elem} and ν_{elem} are accordingly the mesoscopic elastic modulus and Poisson's ratio of the element (mortar, aggregate or reinforcement), which can be derived from the macroscale material properties as Eq. (4.2).

$$\begin{cases} Ksp_n = Ksp_\varphi = \frac{(1 - \nu_{elem})E_{elem}}{(1 + \nu_{elem})(1 - 2\nu_{elem})} \\ Ksp_s = \frac{E_{elem}}{2(1 + \nu_{elem})} \end{cases} \quad (4.1)$$

$$\begin{aligned} \nu_{elem} &= -24.8v^4 + 31.9v^3 - 16.4v^2 + 4.28v \\ E_{elem} &= E \left(-33.7\nu_{elem}^4 + 17.0\nu_{elem}^3 - 4.13\nu_{elem}^2 + 0.327\nu_{elem} + 1 \right) \end{aligned} \quad (4.2)$$

For normal and shear springs of mortar-aggregate interface, the stiffness K is given as weighted average of mortar and aggregate like mesoscale 2D RBSM, as shown in Eq. (2.2). In which, h

is the length of the perpendicular line from the centroid of element to the boundary, see **Fig. 4.1**. For normal and shear springs of mortar-reinforcement (bond) interface, the values of stiffness are assumed same as those for mortar according to the suggestion by Muto et al. (2004). It should be emphasized that for circumferential springs, the values of stiffness for mortar-reinforcement (bond), mortar-mortar, mortar-aggregate (ITZ) and aggregate-aggregate interfaces are calculated using E_{elem} and ν_{elem} of mortar. In other words, the circumferential springs of concrete have the elastic modulus and Poisson's ratio as mortar for simplification, no matter they are located in mortar, aggregate, ITZ or bond interface on the z-r plane.

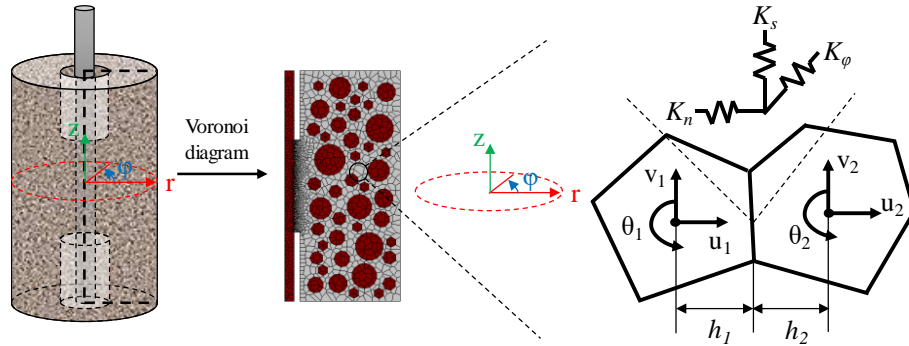


Fig. 4.1. Schematic of mesoscale axisymmetric RBSM model

Other definitions are same with 2D mesoscale plane stress RBSM as described in section 2.1 except for following points:

(1) for the shear springs of mortar, the value of maximum shear strength τ_{max} changes based on the status of normal springs follow Eq. (4.3) like 3D RBSM (Nagai et al. 2005):

$$\tau_{max} = \pm \left(0.30 f_{t_{elem}}^{2.5} (-\sigma + f_{t_{elem}})^{0.4} + 0.15 f_{t_{elem}} \right) \quad (4.3)$$

(2) for circumferential springs of mortar-reinforcement (bond), mortar-mortar, mortar-aggregate (ITZ) and aggregate-aggregate interfaces, the values of tensile strength are set the same as ITZ for consideration that ITZ usually acts as the weakest part and dominates the circumferential behaviors.

4.1.2 Development of stiffness matrix

To develop the mesoscale axisymmetric RBSM, the stiffness matrix is rather important, and

the following process shows how to derive it:

Firstly, define $\mathbf{u}=[u_{P1} \ v_{P1} \ u_{P2} \ v_{P2}]^T$ and $\mathbf{u}_e=[u_1 \ v_1 \ \theta_1 \ u_2 \ v_2 \ \theta_2]^T$ to be the displacement vectors of mid-point of interface between two adjacent elements (point **P**) and elemental centroids (point **1** and **2**) in global z-r-φ polar coordinate system, see **Fig. 4.2**.

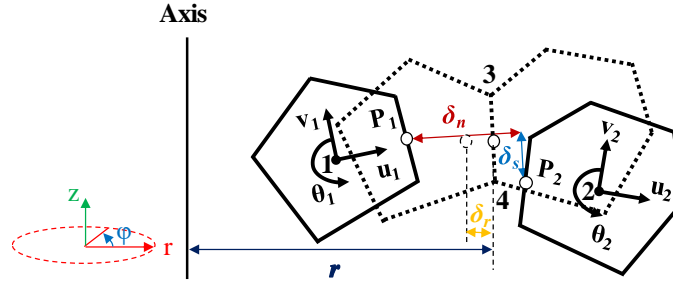


Fig. 4.2 Illustration of two adjacent elements in axisymmetric RBSM

Then the relationship between \mathbf{u} and \mathbf{u}_e is given as Eq. (4.4), where $x_{ij}=x_i-x_j$ and $y_{ij}=y_i-y_j$; $\mathbf{0}$ is the zero matrix:

$$\mathbf{u} = \mathbf{Q} \cdot \mathbf{u}_e$$

$$\mathbf{Q} = \begin{bmatrix} 1 & 0 & y_P - y_1 & \mathbf{0} \\ 0 & 1 & -(x_P - x_1) & \mathbf{0} \\ \mathbf{0} & \mathbf{0} & 1 & 0 & y_P - y_2 \\ \mathbf{0} & \mathbf{0} & 0 & 1 & -(x_P - x_2) \end{bmatrix} = \begin{bmatrix} 1 & 0 & y_{P1} & \mathbf{0} \\ 0 & 1 & -x_{P1} & \mathbf{0} \\ \mathbf{0} & \mathbf{0} & 1 & 0 & y_{P2} \\ \mathbf{0} & \mathbf{0} & 0 & 1 & -x_{P2} \end{bmatrix} \quad (4.4)$$

Converting the displacement of point **P** from global polar coordinate system (z-r-φ) into local orthogonal coordinate system (n-s) where normal and shear springs locate, it yields that:

$$\underline{\mathbf{u}} = \mathbf{R} \cdot \mathbf{u}$$

$$\mathbf{R} = \begin{bmatrix} \cos \theta_n & \sin \theta_n & \mathbf{0} \\ -\sin \theta_n & \cos \theta_n & \mathbf{0} \\ \mathbf{0} & \mathbf{0} & \cos \theta_n & \sin \theta_n \\ \mathbf{0} & \mathbf{0} & -\sin \theta_n & \cos \theta_n \end{bmatrix} = \frac{1}{L_{43}} \begin{bmatrix} -y_{43} & x_{43} & \mathbf{0} \\ -x_{43} & -y_{43} & \mathbf{0} \\ \mathbf{0} & \mathbf{0} & -y_{43} & x_{43} \\ \mathbf{0} & \mathbf{0} & -x_{43} & -y_{43} \end{bmatrix} \quad (4.5)$$

where $\underline{\mathbf{u}}=[\underline{u}_{P1} \ \underline{v}_{P1} \ \underline{u}_{P2} \ \underline{v}_{P2}]^T$ is the displacement vector of point **P** in local coordinate system. θ_n stands for the angle between interface and *r*-direction. L_{43} represents the length between point **3** and **4**, as shown in **Fig. 4.2**. Once the displacements of point **P** are given, the spring deformation vector $\mathbf{d}=[\delta_n \ \delta_r \ \delta_s]^T$ of point **P** could be calculated, referring to Eq. (4.6). δ_n and δ_s represent the deformation of normal and shear springs. δ_r stands for the deformation in *r*-

direction, which in other words, is the translational movement of point **P** towards the z-axis, see **Fig. 4.2**.

$$\mathbf{d} = \mathbf{M} \cdot \mathbf{u}$$

$$\begin{Bmatrix} \delta_n \\ 2\delta_r \\ \delta_s \end{Bmatrix} = \begin{bmatrix} -1 & 0 & 1 & 0 \\ \cos \theta_n & -\sin \theta_n & \cos \theta_n & -\sin \theta_n \\ 0 & -1 & 0 & 1 \end{bmatrix} \begin{Bmatrix} \underline{u}_{P1} \\ \underline{v}_{P1} \\ \underline{u}_{P2} \\ \underline{v}_{P2} \end{Bmatrix} = \begin{bmatrix} -1 & 0 & 1 & 0 \\ \frac{-y_{43}}{l_{43}} & \frac{-x_{43}}{l_{43}} & \frac{-y_{43}}{l_{43}} & \frac{-x_{43}}{l_{43}} \\ 0 & -1 & 0 & 1 \end{bmatrix} \begin{Bmatrix} \underline{u}_{P1} \\ \underline{v}_{P1} \\ \underline{u}_{P2} \\ \underline{v}_{P2} \end{Bmatrix} \quad (4.6)$$

Combing Eq. (4.4), (4.5) and (4.6), it indicates that the relationship between $\mathbf{u}_e = [u_1 \ v_1 \ \theta_1 \ u_2 \ v_2 \ \theta_2]^T$ and $\mathbf{d} = [\delta_n \ \delta_r \ \delta_s]^T$ follows:

$$\mathbf{d} = \mathbf{N} \cdot \mathbf{u}_e$$

$$\mathbf{N} = \mathbf{M} \cdot \mathbf{R} \cdot \mathbf{Q} = \frac{1}{l_{43}} \begin{bmatrix} y_{43} & -x_{43} & x_{43}x_{P1} + y_{43}y_{P1} & -y_{43} & x_{43} & -x_{43}x_{P2} - y_{43}y_{P2} \\ \frac{l_{43}}{2} & 0 & \frac{l_{43}y_{P1}}{2} & \frac{l_{43}}{2} & 0 & \frac{l_{43}y_{P2}}{2} \\ x_{43} & y_{43} & x_{43}y_{P1} - y_{43}x_{P1} & -x_{43} & -y_{43} & -x_{43}y_{P2} + y_{43}x_{P2} \end{bmatrix} \quad (4.7)$$

The relationship between spring deformation vector $\mathbf{d} = [\delta_n \ \delta_r \ \delta_s]^T$ and spring strain vector $\boldsymbol{\varepsilon} = [\varepsilon_n \ \varepsilon_\varphi \ \varepsilon_s]^T$ follows Eq. (4.8):

$$\boldsymbol{\varepsilon} = \begin{Bmatrix} \varepsilon_n \\ \varepsilon_\varphi \\ \varepsilon_s \end{Bmatrix} = \begin{Bmatrix} \delta_n / (h_1 + h_2) \\ \delta_r / r \\ \delta_s / (h_1 + h_2) \end{Bmatrix} = \mathbf{B} \cdot \mathbf{u}_e \quad (4.8)$$

$$\mathbf{B} = \frac{1}{l_{43}} \begin{bmatrix} y_{43}/h & -x_{43}/h & (x_{43}x_{P1} + y_{43}y_{P1})/h & -y_{43}/h & x_{43}/h & (-x_{43}x_{P2} - y_{43}y_{P2})/h \\ \frac{l_{43}}{2r} & 0 & \frac{l_{43}y_{P1}}{2r} & \frac{l_{43}}{2r} & 0 & \frac{l_{43}y_{P2}}{2r} \\ x_{43}/h & y_{43}/h & (x_{43}y_{P1} - y_{43}x_{P1})/h & -x_{43}/h & -y_{43}/h & (-x_{43}y_{P2} + y_{43}x_{P2})/h \end{bmatrix}$$

where h_i is the length of the perpendicular line from the centroid of element to the boundary ($h = h_1 + h_2$), see **Fig. 4.1**. r is the radial distance between point **P** and the axis, see **Fig. 4.2**.

According to the theories of mechanics of elastic bodies, the stress-strain relationship for springs in axisymmetric model is:

$$\begin{Bmatrix} \sigma_n \\ \sigma_\varphi \\ \sigma_s \end{Bmatrix} = \mathbf{D} \cdot \begin{Bmatrix} \varepsilon_n \\ \varepsilon_\varphi \\ \varepsilon_s \end{Bmatrix} = \begin{bmatrix} \frac{(1-\nu)E}{(1+\nu)(1-2\nu)} & 0 & 0 \\ 0 & \frac{(1-\nu)E}{(1+\nu)(1-2\nu)} & 0 \\ 0 & 0 & \frac{E}{2(1+\nu)} \end{bmatrix} \begin{Bmatrix} \varepsilon_n \\ \varepsilon_\varphi \\ \varepsilon_s \end{Bmatrix} \quad (4.9)$$

In Eq. (4.9), σ and ε means stress and strain, and subscripts n , s and φ represent normal, shear and circumferential direction, respectively. Applying the principle of virtual work, if small

displacement \mathbf{u}_e^* is assumed to take place on the adjacent elements, the corresponding strain of springs would be $\boldsymbol{\varepsilon}^*$:

$$\{\mathbf{u}_e^*\}^T \cdot \mathbf{f}_e = \int \{\boldsymbol{\varepsilon}^*\}^T \cdot \boldsymbol{\sigma} \quad (4.10)$$

where \mathbf{f}_e is the force vector of element centroids (point **1** and **2**). Considering the spring lengths and effective areas, the right term of Eq. (4.10) could be transformed according to Eq. (4.8) and (4.9):

$$\int \{\boldsymbol{\varepsilon}^*\}^T \cdot \boldsymbol{\sigma} = \{\mathbf{B} \cdot \mathbf{u}_e^*\}^T \begin{bmatrix} h_1+h_2 & 0 & 0 \\ 0 & 2\pi r & 0 \\ 0 & 0 & h_1+h_2 \end{bmatrix} \cdot \begin{bmatrix} l_{43} \times 2\pi r & 0 & 0 \\ 0 & l_{43} \times (h_1+h_2) & 0 \\ 0 & 0 & l_{43} \times 2\pi r \end{bmatrix} \mathbf{D} \cdot \mathbf{B} \cdot \mathbf{u}_e \quad (4.11)$$

Substitute Eq. (4.11) into Eq. (4.10) and eliminate the term of $\{\mathbf{u}_e^*\}^T$, it yields that:

$$\begin{aligned} \mathbf{f}_e &= 2\pi r l_{34} (h_1+h_2) \cdot \mathbf{B}^T \mathbf{D} \mathbf{B} \cdot \mathbf{u}_e = \mathbf{K} \cdot \mathbf{u}_e \\ \mathbf{K} &= 2\pi r l_{34} (h_1+h_2) \cdot \mathbf{B}^T \mathbf{D} \mathbf{B} \end{aligned} \quad (4.12)$$

Finally, the stiffness matrix \mathbf{K} is derived for axisymmetric mesoscale Rigid Body Spring Method. Afterwards, the micro-meso strengthening/damaging models accounting for ice formation in porous material were integrated into the normal and circumferential springs of newly-developed program.

4.2 Verification of Axisymmetric RBSM

After the mesoscale axisymmetric RBSM had been developed, two sorts of tests were adopted to verify its reliability and applicability including the uniaxial compression test of pure concrete (intact and damaged) and uniaxial tensile test of reinforcement. For compression of pure concrete, results from 2D mesoscale RBSM and experiment were compared with axisymmetric mesoscale RBSM. While for tension of reinforcement, the elastic modulus and Poisson's ration of steel bar were investigated. Details are stated in the following.

4.2.1 Uniaxial compression of concrete

Cylindrical concrete specimens were modeled according to the NC-C35 specimens in the experiment by Liu et al. (2016) where no air-entraining-agent was used. Compressive strength of non-damaged concrete was 39.28 MPa and the mix proportion was listed in **Table 4.1**. As stated in previous chapters, some mesoscale material inputs can be calculated once others were

given, see Eq. (2.9). It is indicated from Eq. (2.9) that the strength of ITZ was always less than that of mortar, which means the ITZ acted as the weakest part. Besides, as mentioned in section 4.1.1, the stiffness of bond interface was set same with that of mortar while the stiffness of ITZ between mortar and aggregate is assumed as the weight averaged value between two materials. Thus, mortar-aggregate interface was always stiffer than the bond interface. Volume fraction of aggregate was determined by the proportion of concrete and density of aggregate. Same as the 2D RBSM, size distribution was calculated as the suggestion by JSCE standard. The dimension of concrete specimens is $\Phi 100 \times 200 \text{ mm}^2$. Each model was modeled both by 2D plane stress RBSM and axisymmetric RBSM respectively, see Fig. 4.3.

Table 4.1. Mix proportion of concrete (Liu et al. 2016)

Type	Cement (kg/m ³)	Water (kg/m ³)	Sand (kg/m ³)	GHB* (kg/m ³)	Gravel (kg/m ³)	w/c
C30	239	127	490	156	970	0.53
C35	384	192	468	156	986	0.50
C40	417	200	440	156	1010	0.48

Note: *-In calculation of material inputs, GHB was neglect for NC-C35 specimens while GHB was assumed as coarse aggregate for TIC specimens, as shown in section 4.2.3.

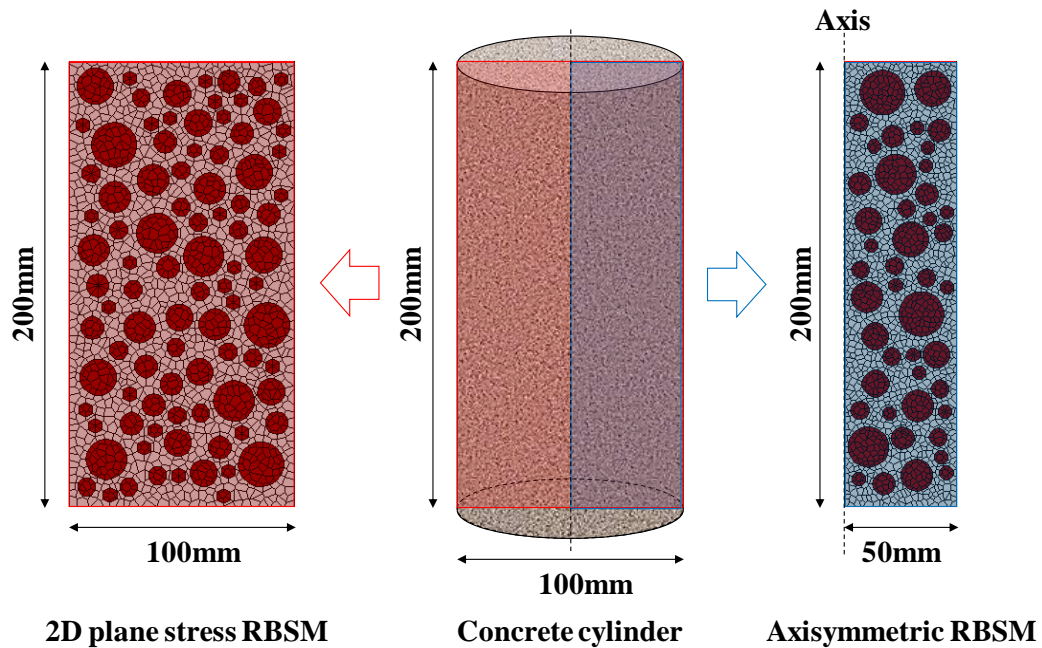


Fig. 4.3. Cylindrical concrete, 2D plane stress RBSM and axisymmetric RBSM

FTC was firstly applied to the (2D and axisymmetric) models before the external compressive loading. Simplification was made to neglect the effect of freezing and thawing rates so that much less computation time was consumed, as explained in previous chapter 3. Previous works had proved that such simplification would not affect the simulation results of final status of the frost-damaged specimens, which was the focus. According to Liu et al. (2016), the temperature variation was from +20°C to -20°C in one cycle and three cases were prepared depending on different number of cycles (30, 60 and 100). The temperature was applied uniformly to the specimen without considering the thermal lag effect (Wang et al. 2017). After the FTC, prescribed displacement loading with 0.005 mm/step was applied vertically to the top surface of frost-damaged models. Meanwhile, restrictions of horizontal, vertical and rotational direction were given to the bottom surface of the specimens. The analytical compressive stress-strain curves for both intact and frost-damaged concrete were drawn in **Fig. 4.4**, where “2D” and “Axi” represented the simulation results with 2D plane stress RBSM and axisymmetric RBSM, respectively; The numbers (0, 30, 60 and 100) stood for the numbers of freezing and thawing cycles. From **Fig. 4.4**, it indicated that the two different models had satisfactory agreements in different aspects, e.g. compressive strength, strain at peak compressive stress as well as the stiffness in ascending branches. However, post-peak behaviors showed slightly different between 2D and axisymmetric simulation. The reason was that after cracks initiated in normal springs in x-y or z-r plane, these in-plane springs in 2D model became free to move while the in-plane springs in axisymmetric model could still be confined by the circumferential springs. The cracking patterns of sound concrete by both models were drawn in **Fig. 4.5** where **(a)** and **(d)** showed the original models before compressive loading; **(b)** and **(c)** showed the post peak deformations where the deformations were enlarged by 10 times; **(e)** and **(f)** represented the cracking patterns in z-r plane where the red short lines meant the stress of normal spring had reached zero and become ineffective to sustain any load (strain of normal springs equaled to ε_{\max} in **Fig. 2.4** and **2.5**, and the crack width could be calculated according to the length of spring). As already known, typical X-shape cracking was observed in 2D plane stress case as shown in **Fig. 4.5(c)**. Besides, the cracking shape could also be simulated with axisymmetric model, see **Fig. 4.5(f)**. It should be emphasized that the cracking of circumferential springs (in

ϕ direction) was plotted in **Fig. 4.5(g)** where the blue spots meant that the strain of circumferential springs had reached ε_{\max} . Compared with 2D plane stress RBSM, axisymmetric RBSM could give more information since it dealt with the issues of three-dimensional stress condition. In addition, the axisymmetric RBSM needed less computation time than the 2D plane stress RBSM even though it had finer mesh.

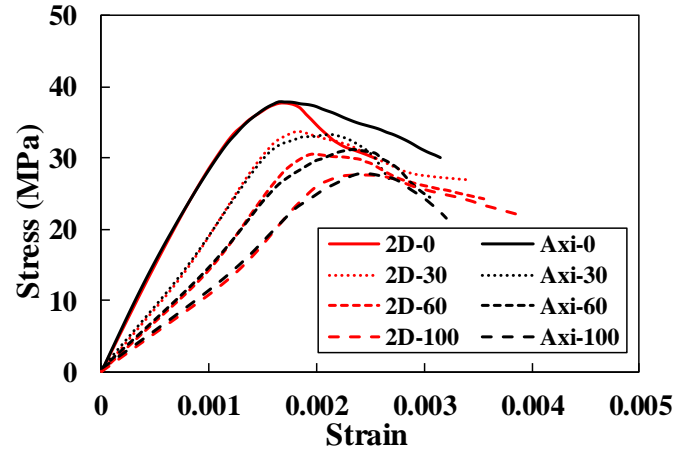


Fig. 4.4. Compressive stress-strain curves by 2D and axisymmetric RBSM

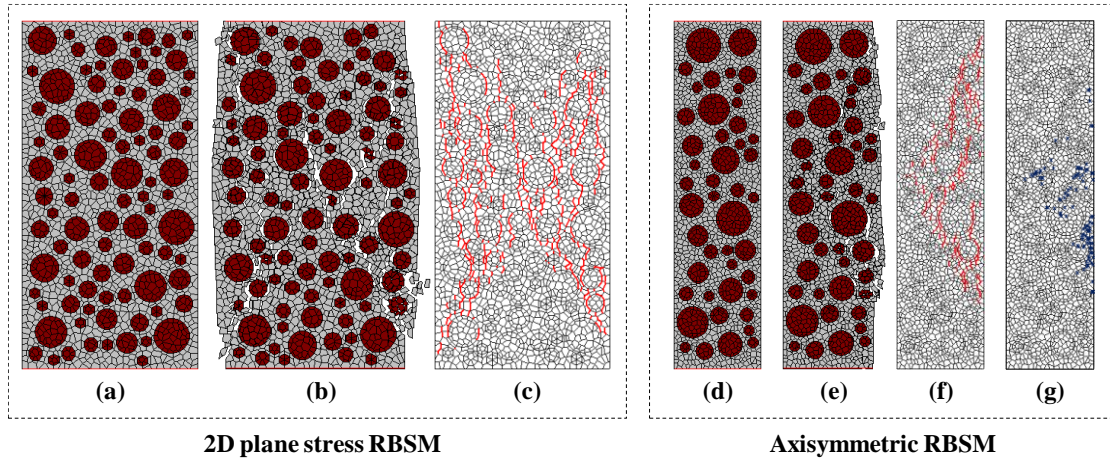


Fig. 4.5. Cracking patterns for sound concrete by 2D and axisymmetric RBSM

Besides, the experimental data of compressive strength degradation by Liu et al. (2016) was also plotted together with the simulation results with both 2D and axisymmetric models, see **Fig. 4.6**. In previous studies, it had already been demonstrated that the 2D plane stress RBSM could successfully predict the deteriorated compressive behaviors of frost-damaged concrete.

Here in **Fig. 4.6** where “2D” and “Axi” represented the simulation results with 2D plane stress RBSM and axisymmetric RBSM, the mesoscale axisymmetric RBSM developed in this study was proved to be reliable and adoptable to predict the material properties of frost-damaged concrete as well.

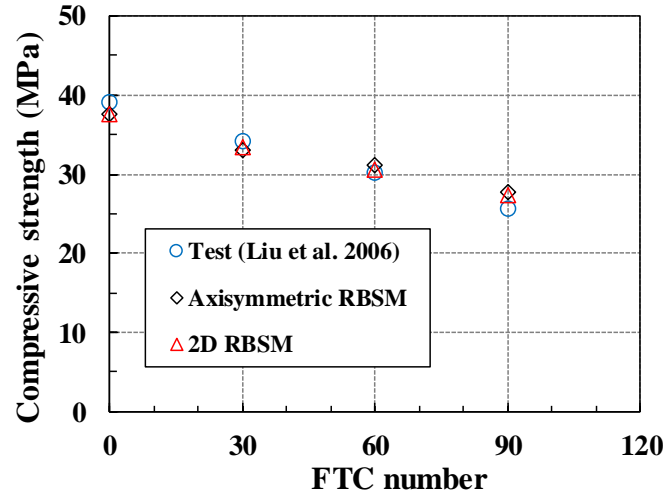


Fig. 4.6. Compressive strength degradation by test, 2D and axisymmetric RBSM

4.2.2 Uniaxial tension of reinforcement

The elastic modulus and Poisson’s ratio of reinforcement was verified by simulating the uniaxial tension test of reinforcement for two reasons: 1. The elastic behaviors of rebar could affect the bond-slip relationship, thus precise simulation of elastic properties of rebar was vital; 2. Owing to the Poisson’s effect, radial contraction of rebar took place when the reinforcement was pulled out of the concrete and longitudinal elongation took place. This radial contraction would lead to delamination between the surface of reinforcement and the covering concrete, which would affect the bond-slip behaviors. As a result, simulation of uniaxial tension was conducted with 200 mm long D12 rebar where the ribs were neglected for simplification, see **Fig. 4.7**. Since it was mentioned that no yielding of rebar was observed in the experiment, no yielding strength was given to the springs for reinforcement in the current program. In other words, only the elastic modulus of rebar was verified and adopted in this simulation. The input elastic modulus and Poisson’s ratio of the reinforcement were 170 GPa and 0.3, respectively.

The simulated results were drawn in **Fig. 4.8** where the calculated elastic modulus and Poisson's ratio were approximately 150 GPa and 0.32, which demonstrated that the elastic behaviors of rebar could be well simulated by the axisymmetric mesoscopic RBSM. Red curve in **Fig. 4.9** showed the calculated Poisson's ratio by simulating the compression test of pure concrete with 2D plane stress RBSM by Nagai et al. (2004). In their study, it had been successfully proved that the Poisson's ration of concrete (around 0.2) could be well simulated with the two-dimensional RBSM. In the current study, the simulation results indicated that the developed axisymmetric RBSM could successfully simulate the Poisson's ratio for reinforcement as well, see the black curve in **Fig. 4.9**.

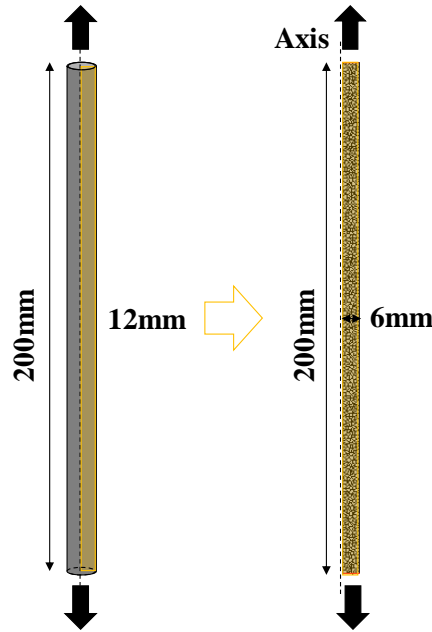


Fig. 4.7. Uniaxial tension test of rebar and axisymmetric RBSM model

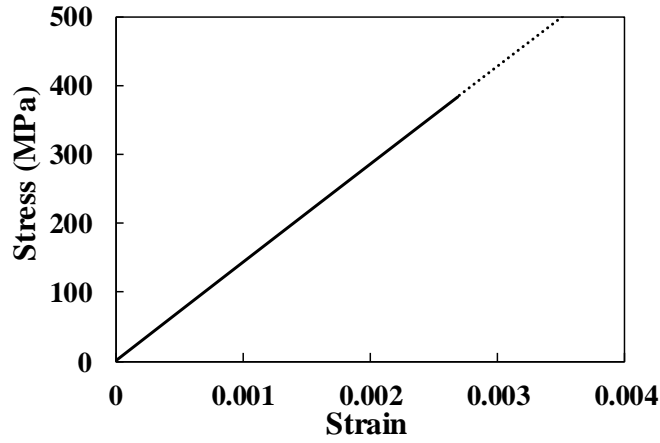


Fig. 4.8. Elastic modulus of reinforcement by axisymmetric RBSM simulation

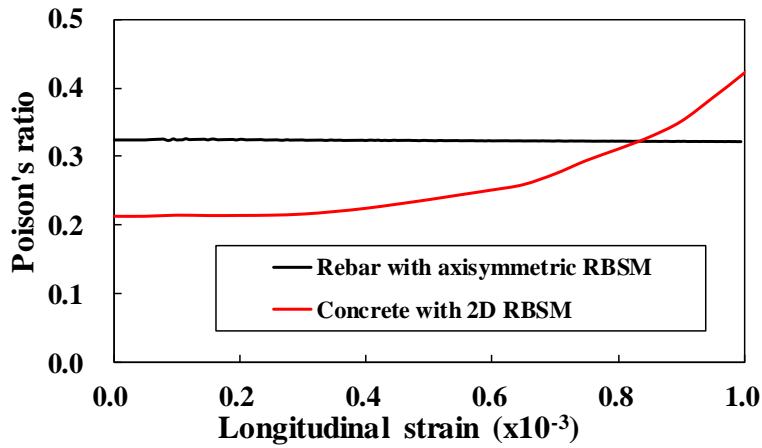


Fig. 4.9. Poisson's of reinforcement by axisymmetric RBSM simulation

4.2.3 Bond-slip of pulling-out specimens

After the simulation of the uniaxial compressive behavior and uniaxial tensile behavior with axisymmetric RBSM had been conducted, the pulling-out test was simulated with both non-damaged and frost-damaged specimens. The model of pulling-out simulation was made following the experimental specimen by Liu et al. (2016): the compressive strength of concrete was 39.28 MPa with proportion listed in **Table 4.1**. One hot-rolled ribbed bar (HRB) with diameter of 12 mm and elastic modulus of 170 GPa was embedded inside of concrete with embedment length equaling to 5D. Since the interlocking mechanisms between ribs of rebar and concrete played a rather important role when deformed reinforcements were adopted, the precise configuration of ribs was also modeled in axisymmetric RBSM. Detailed information

of reinforcement such as cross-sectional area (A_s), spacing between ribs (s_R), rib height (h_R) and rib width (w_R) could be found in previous literature (Liu et al. 2016). For convenience, the values were also listed in **Table 4.2**. The schematic of pulling-out model was drawn in **Fig. 4.10**. In the experiment, plastic sleeves were adopted to insulate the un-bonded region of reinforcement from surrounding concrete so that the desired bond length could be ensured during casting. Besides, water would not penetrate directly from the ends of bond region during FTCs. After curing, the specimens were put into containers with 5 mm demineralized water of immersion where water could only penetrate from the surfaces (top, bottom and side surfaces) of concrete. As a result, an un-bonded area was modeled in the RBSM program as well, as shown in **Fig. 4.10**.

Table 4.2. Morphology of HRB-D12 reinforcement (Liu et al. 2016)

Type	A_s (mm ²)	s_R (mm)	h_R (mm)	w_R (mm)
HRB $\Phi 12$	113.1	7.9	0.99	1.0

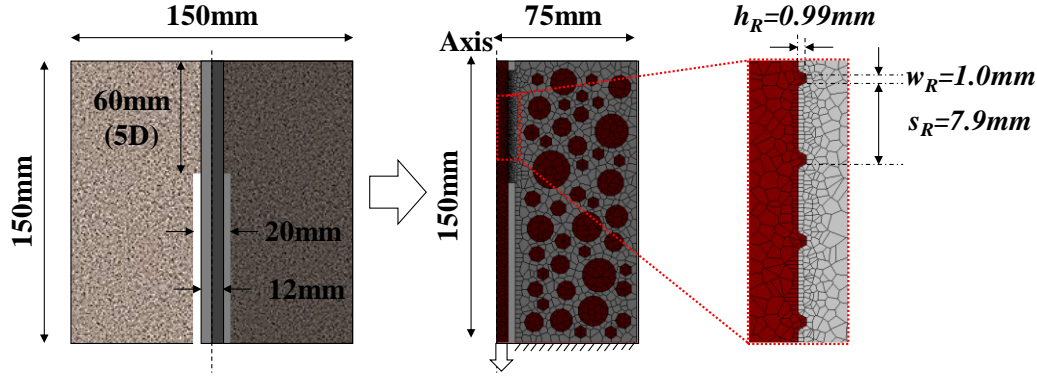


Fig. 4.10 Axisymmetric pulling-out model and details of ribs

It should be emphasized that Liu et al. (2016) also prepared several thermal insulation pulling-out specimens with different embedment length (3D and 6.5D) and concrete strength (C30 and C40) by casting the concrete with additional glazed hollow beads (GHB). Although the frost-damage resistance of such specimens was somehow difficult to simulate in current study, simulating the pulling-out behaviors of those non-damaged specimens could offer more support to the reliability of the program. Accordingly, for the intact pulling-out models, five

cases were simulated depending on the embedment length (3D, 5D and 6.5D) and concrete strength (C30, C35 and C40), see **Table 4.3**. To model those thermal insulation specimens, the GHB was treated as aggregate as explained in **Table 4.1** as well. In **Table 4.3**, the models were named by “concrete strength grade-embedment length-FTC numbers”. For instance, “C35-5D-30” meant that the specimen was made of C35 (compressive strength=39.28 MPa) concrete and the embedment of reinforcement was 5D (60 mm) which had suffered from 30 freezing and thawing cycles. Material inputs could be calculated according to Eq. (2.9) and FTC followed the same process as described in section 2.2. Similar to the simulation in section 4.2.1, three damage levels were prepared where FTC stopped at the end of 30, 60 and 100 cycles together with one reference case. Pulling-out simulation was conducted after the specimens had finished the corresponding numbers of FTCs. Prescribed displacement loading with 0.01 mm/step was applied vertically at the bottom surface of reinforcement while the bottom surface of concrete was restrained in horizontal, vertical and rotational directions, see **Fig. 4.10**.

The average bond stress τ was calculated by Eq. (4.13) where P , D and l_a was the applied load, rebar diameter and anchorage length. The bonding area was directly calculated imaging a plain rebar. In other words, the area contribution from ribs was neglected. The slip between reinforcement and concrete was defined as the displacement of the loading end (bottom surface of the reinforcement). The bond-slip behaviors of non-damaged specimens were drawn in **Fig. 4.11**. From **Fig. 4.11**, it was indicated that for same concrete strength (C35), the calculated bond strength showed slightly decreasing with larger embedment length. Meanwhile, for specimens with the same embedment length (5D), the bond strength would increase by increasing the concrete strength grade. This phenomenon matched well with the observation by Liu et al. (2016) and other studies.

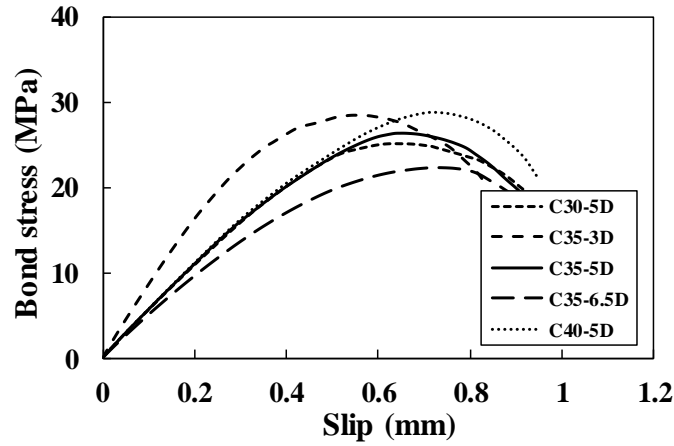


Fig. 4.11. Bond stress-slip curves of non-damaged specimens by axisymmetric RBSM

The bond strength for all the models (both intact and frost-damaged case) were listed in **Table 4.3** and plotted together with the experimental results, as shown in **Fig. 4.12**. Though the simulated bond strength showed a bit larger than the test data, but they were still considered to be correlated since the experimental results also showed larger scattering (up to 24.8%) according to Liu et al. (2016).

$$\tau = \frac{P}{\pi d l_a} \quad (4.13)$$

Table 4.3. Bond strength by Liu et al. (2016) and RBSM

Specimens	τ_u (MPa)		Cov. (%)
	Test	RBSM	
C30-5D	22.35	25.14	11.09
C35-3D	26.85	28.34	5.26
C35-5D	24.80	26.41	6.09
C35-6.5D	22.70	22.29	2.12
C40-5D	26.43	28.83	8.32
C35-5D-30	22.42	24.04	6.73
C35-5D-60	20.67	21.35	3.18
C35-5D-100	15.94	15.93	0.06

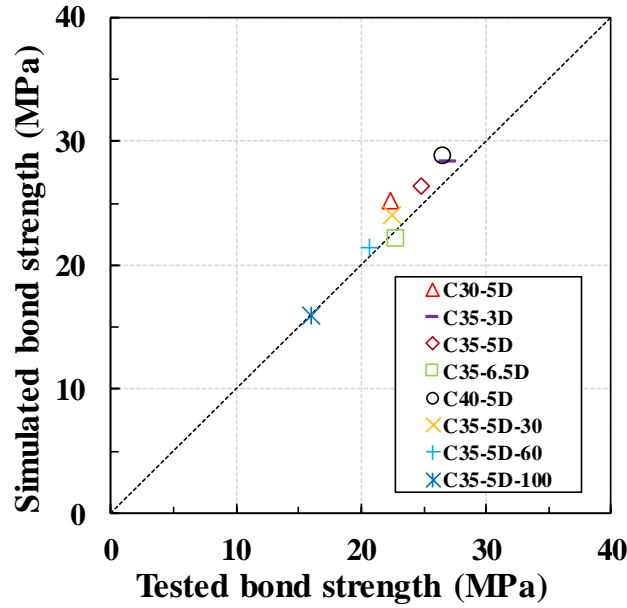


Fig. 4.12. Comparison of bond strength by experiment and axisymmetric RBSM

The deformations and meso-cracks of all the models after suffering different freezing-thawing cycles were drawn in **Fig. 4.13** and **4.14**, where the deformations in **Fig. 4.13** were enlarged by 100 times and the short red lines in **Fig. 4.14** represented the crack width of the corresponding normal spring had reached 0.005 mm. From **Fig. 4.13** and **4.14**, it yielded that the frost action would lead to meso-cracks and expansive deformations in concrete (as chapter 3). Besides, meso-cracks initiated firstly along ITZ and bond regions since they acted as the weakest parts. Especially for the specimen suffering 100 FTCs, obvious meso-cracks could be found between reinforcement and concrete, see **Fig. 4.13(d)** and **Fig. 4.14(d)**, which would diminish the bond strength in a large extent. It should be also emphasized that since the spring length of bond interface was less than that of ITZ between mortar and aggregate, the tensile strain (damage) of bond interface was larger than that of ITZ between mortar and aggregate.

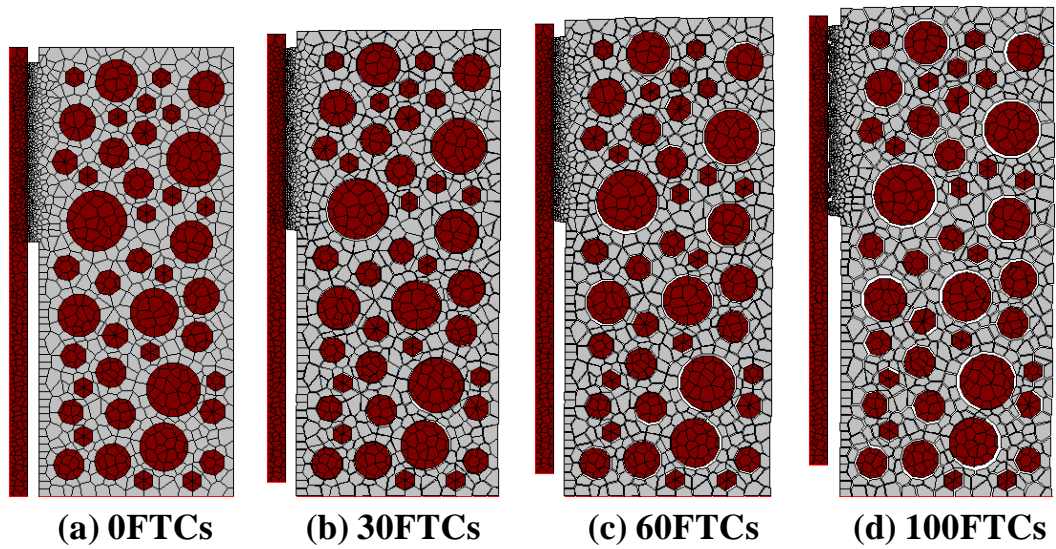


Fig. 4.13. Deformations of the specimens after FTCs (enlarged by 100 times)

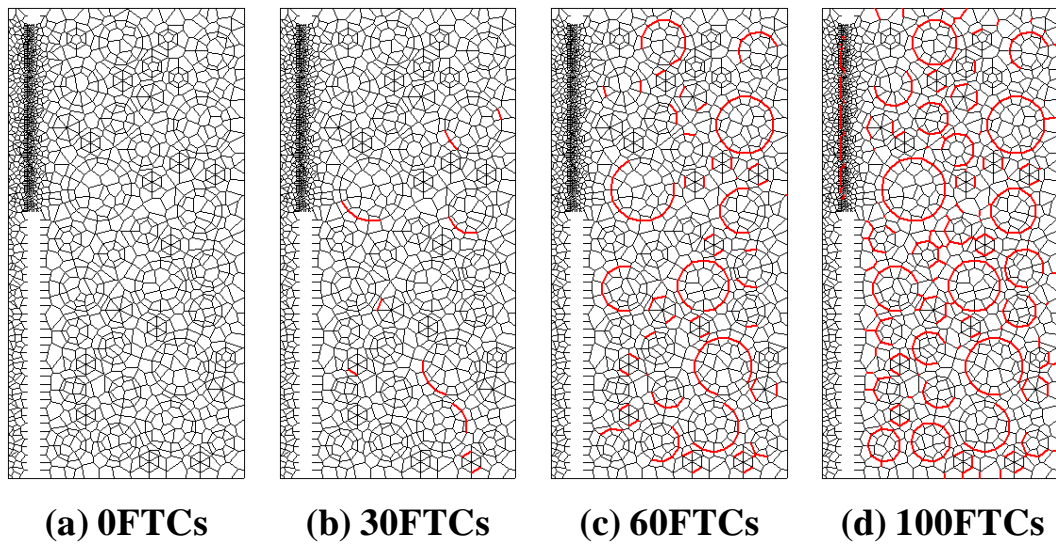


Fig. 4.14. Meso-cracks (=0.005 mm) of the specimens after FTCs

The simulated bond-slip behaviors of frost-damaged models were drawn in **Fig. 4.15** and the degradation of bond strength were plotted in **Fig. 4.16** together with the experimental results. It was indicated that the frost damage had obvious influence on the bond-slip behaviors: both bond strength and stiffness showed significant reduction with increasing numbers of freezing-thawing cycles while the slip at peak bond stress increased slightly in the first few FTCs and decreased later. The slip at peak bond stress showed different behaviors in meso-macro simulations compared with previous experimental results, which needed further examinations.

From **Fig. 4.16** where the analytical and experimental results were plotted and compared, correlation between the RBSM simulation and experimentation could be found on the degradation of bond strength, which strongly demonstrated the fact that the developed program could predict the degradation of bond strength under the effect of frost damage.

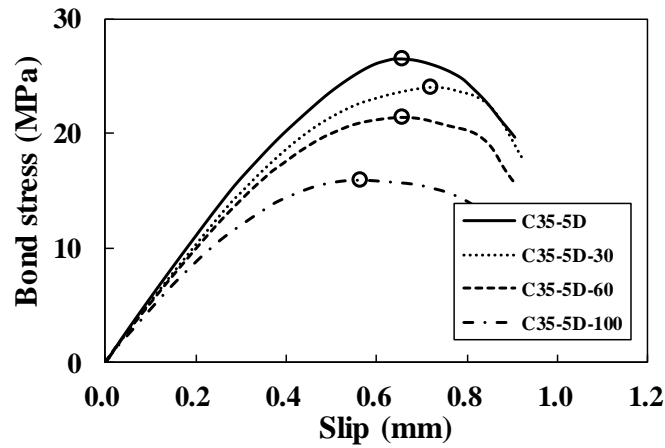


Fig. 4.15. Bond stress-slip curves for both sound and damaged specimens by RBSM

The cracking patterns in z-r plane when normal springs reached the maximum bond stress were shown in **Fig. 4.17**, where the short red lines meant that the width of cracks had reached 0.005 mm in the corresponding normal springs. From **Fig. 4.17**, with more cycles of freezing-thawing, the diagonal cracks induced by external load would penetrate deeper into concrete from bond interface. These cracks would connect with the meso-cracks in concrete which were generated by the frost action, see **Fig. 4.17(d)**.

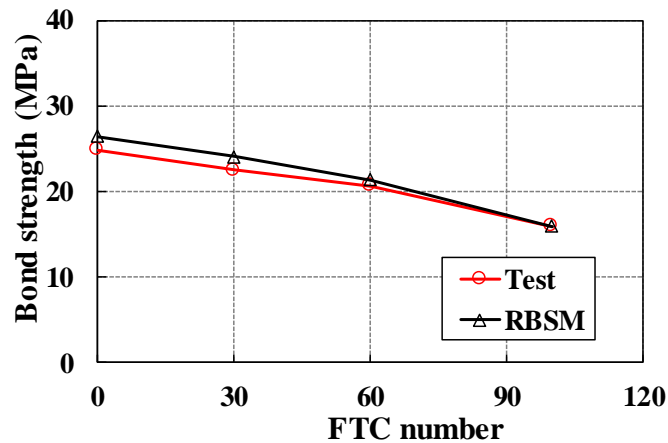


Fig. 4.16. Comparison of bond strength degradation between experiment and RBSM

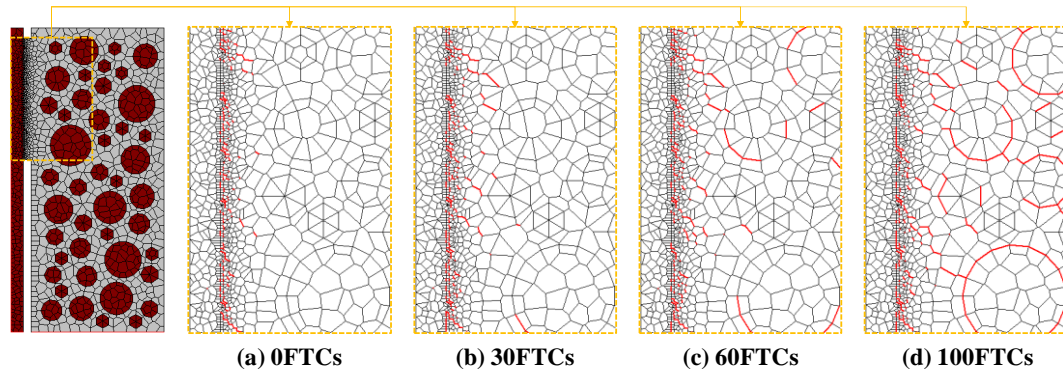


Fig. 4.17. Cracking patterns of the specimens at maximum bond stress

4.3 Simulation and Modeling of Bond

4.3.1 Meso-macro simulation

The bond behavior between concrete and reinforcement under the effect of frost damage was simulated and modeled using the axisymmetric mesoscale RBSM. Two models with different water cement ratio were made ($w/c=0.42$ and 0.52). Each model was further categorized depending on the the minimum temperature in each FTC ($T_{\min}=-10, -20, \text{ and } -30\text{ }^{\circ}\text{C}$) and the number of cycles ($N=30, 60 \text{ and } 100$). In addition, a reference model without any frost damage was simulated for comparison. The schematic of pulling-out model was same as the one shown in **Fig. 4.10**, where the dimension of concrete was $75 \times 150\text{ mm}^2$ with volume fraction of coarse aggregate equaling to 40%. The grain size distribution followed the suggestion by JSCE standard. Deformed steel bar with the nominal diameter of 12 mm was embedded in the concrete with bond length of 5D (60 mm). Detailed information of rebar such as the configuration of ribs was shown in **Fig. 4.10**. The elemental size of mortar and aggregate was approximately 4.5 mm while the size of reinforcement elements was around 2 mm. Besides, finer mesh in gradient (from 0.5 mm to 2 mm) was adopted near the bond area. The specimens were tested with pulling-out load after suffering a whole process of FTC. Prescribed displacement loading was adopted downwardly at the bottom surface of the reinforcement while the bottom surface of the concrete was restrained in horizontal, vertical and rotational

directions. Similarly, the material inputs were calculated according to Nagai et al. (2004) and Gong et al. (2017), see **Table 4.4**.

Table 4.4. Material inputs for pulling-out models with different w/c

w/c	f_{cm}' (Mpa)	E_m (MPa)	f_{tp} (MPa)	f_{ti} (Mpa)	c_i (Mpa)	ϕ
0.42	40.0	22904.37	3.66	1.69	2.81	0.186
0.52	30.0	20689.22	3.26	1.55	2.54	0.225

4.3.2 Modeling of deteriorated bond-slip relationship

Some experimental studies had suggested to model the bond degradation by relating the bond strength with relative dynamic elastic modulus. In this study, relative compressive strength of concrete was adopted as the damage indicator instead of RDEM for consideration of the consistency with material degradation models of concrete as stated in chapter 3. Empirical model for deteriorated bond strength was proposed based on the simulation results, as Eq. (4.14), where τ_l and τ_{ld} represented the bond strength for sound and frost-damaged specimens, respectively. In meso-macro simulations, pulling-out failure in bond area instead of splitting crack of covering concrete was found for all models. The deteriorated bond strength by Eq. (4.14) was compared with several test data as shown in **Fig. 4.18** where good correlation could be found. To model the bond-slip relationship, the expression of intact case suggested by fib Model Code 2010 was adopted and modified for the frost-damaged case: The bond strength τ_l , residual bond strength τ_3 and corresponding slip values (s_1 , s_2 and s_3) for non-damaged case could be adopted following fib Model Code 2010; For frost-damaged case, the bond strength τ_l could be calculated by Eq. (4.14) and the residual bond strength τ_3 was assumed to be reduced proportionally to the bond strength τ_l . According to Hanjari et al. (2011), the corresponding slip values (s_1 , s_2 and s_3) for frost-damaged case were simply assumed the same as non-damaged case. Comparison between the analytical bond-slip relationship by Eq. (4.14) and test results was made in **Fig. 4.19**.

$$\tau_{ld} = (1.259Rf_c - 0.259)\tau_l \quad (4.14)$$

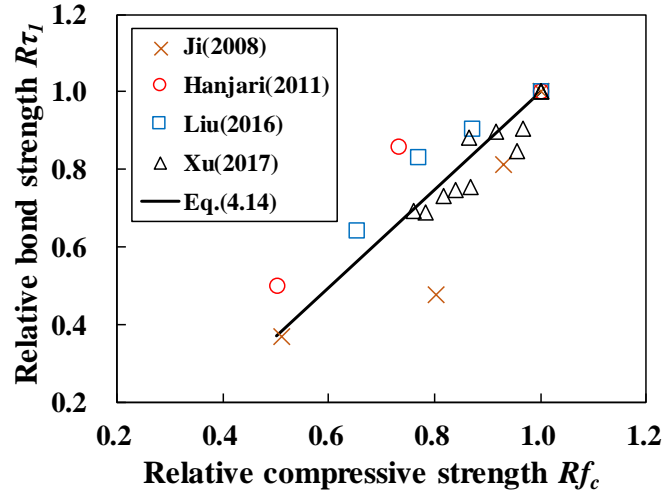


Fig. 4.18. Comparison of $R\tau_l$ between proposed model and experiments

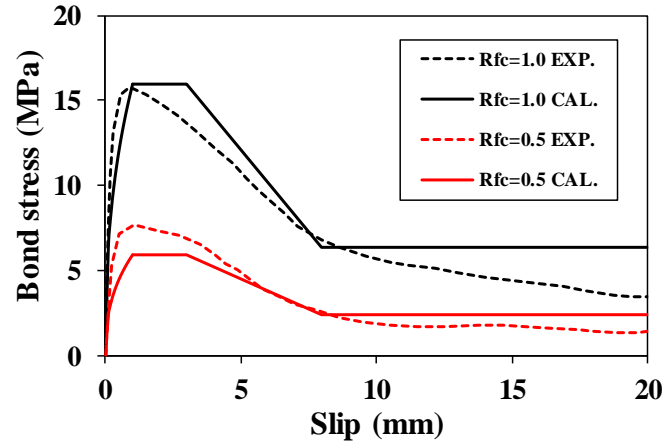


Fig. 4.19. Comparison between experimental and analytical bond-slip curves

4.4 Conclusions of This Chapter

Following conclusions could be drawn from current chapter:

- (1) The axisymmetric mesoscale Rigid Body Spring Method program was successfully developed by derivation of stiffness matrix and programming work. Through combining the micro-meso strengthening/damaging models accounting for frost action in chapter 3, the pulling-out behaviors of specimens of short embedment length with frost damage was analyzed.
- (2) Simulations of uniaxial compression of pure concrete and uniaxial tension of rebar were conducted. It yielded the axisymmetric RBSM could simulate the mechanical behavior of

concrete (both intact and with frost-damage) and reinforcement (both elastic modulus and Poisson's ratio) well, which demonstrated the reliability and applicability of the program.

(3) Pulling-out test of short embedment specimens was simulated and analyzed with the new program. For non-damaged specimens, the macroscale bond-slip behaviors could be well simulated with different cases (e.g. concrete strength and embedment length), which further showed the reliability of the program. For frost-damaged specimens, the degradation of bond strength by meso-macro simulation was observed in good correlation with experimental data.

(4) Parametric study was conducted to propose the bond deterioration model based on the meso-macro simulation results, which was hopefully to be adopted in the structural analysis with Finite Element Method.

References

- A. Kambayashi, H. Kobayashi, K. Sonoda, Applicability of a rigid body spring model to impact problems of axi-symmetric elastic bodies, *Journal of Applied Mechanics*. 2 (1999) 271-278.
- B. Yao, W. Murray, Study of concrete cracking and bond using a distributed discrete crack finite element model, *ACI Materials Journal*. 92 (1) (1995) 93-104.
- N. Takeuchi, M. Ueda, T. Kawai, An analysis of axisymmetric problems by means of new discrete models, *Kenkyu Sokuho*. 32 (6) (1980) 31-34.
- S. Muto, H. Nakamura, T. Tanabe, W. Srisoros, S. Lee, Analysis of bond characteristics between concrete and deformed bar by meso-scale analysis, *Journal of Applied Mechanics*. 7 (2004) 767-774.
- K. Nagai, Y. Sato, T. Ueda, Mesoscopic simulation of failure of mortar and concrete by 3D RBSM, *Journal of Advanced Concrete Technology*. 3 (3) (2005) 385-402.
- Y. Liu, F. Chen, W. Wang, Z. Li, Bond performance of thermal insulation concrete under freeze-thaw cycles, *Construction and Building Materials*. 104 (2016) 116-125.
- Z. Wang, F. Gong, D. Zhang, H. Hayashida, T. Ueda, Mesoscale simulation of concrete behavior with non-uniform frost damage with verification by CT imaging, *Construction and Building Materials*. 157 (2017) 203-213.
- Japan Society of Civil Engineers, Standard specification for concrete structures, Tokyo: JSCE. (2007).
- K. Nagai, Y. Sato, T. Ueda, Mesoscopic simulation of failure of mortar and concrete by 2D RBSM, *Journal of Advanced Concrete Technology*. 2 (3) (2004) 359-374.
- F. Gong, Y. Wang, T. Ueda, D. Zhang, Modeling and mesoscale simulation of ice-strengthened mechanical properties of concrete at low temperatures, *Journal of Engineering Mechanics*. 143 (6) (2017) 04017022.
- International Federation for Structural Concrete, Fib model code for concrete structures 2010, Berlin: Ernst & Sohn. (2013).
- X. Ji, Y. Song, Y. Liu, Effect of freeze-thaw cycles on bond strength between steel bars and concrete, *Journal of Wuhan University of Technology-Mater. Sci. Ed.* 23 (4) (2008) 584-588.
- K.Z. Hanjari, P. Utgenannt, K. Lundgren, Experimental study of the material and bond

properties of frost-damaged concrete, *Cement and Concrete Research*. 41 (3) (2011) 244-254.

S. Xu, A. Li, H. Wang, Bond properties for deformed steel bar in frost-damaged concrete under monotonic and reversed cyclic loading, *Construction and Building Materials*. 148 (2017) 344-358.

Chapter 5

5. Macroscale Structural Analysis

5.1 Finite Element Analysis

5.1.1 2D heat transfer analysis

According to the literature reviews, “thermal lag” effect exists when dimension of specimen is large which will affect the temperature field inside the reinforced concrete member, thus lead to a different frost damage distribution (Wang et al. 2017). Several factors are related to the thermal lag such as the size of specimen, adopted materials (thermal conductivity), temperature variation speed in freezing and thawing process, ambient humidity, etc. As a result, the temperature field and history during FTC should be understood to precisely calculate the damaged material/bond constitutive relationship. In this study, a simplified heat transfer analysis was conducted without considering the influence from material damage (deformation or crack) on the transfer process. In other words, the thermal conductivity and specific heat capacity was not changing during FTC even though damage was induced. Cross-section of RC beam was modeled and analyzed with 2D FEM application instead of 3D since the longitudinal length of beam was much larger than the dimension of width and height of the beam. DIANA FEA (version 10.2) application was used for the heat flow analysis during FTC and the model of cross0section was shown in **Fig. 5.1(a)**. The thermal conductivity of concrete and rebar was set as constants of 2.67 and 45 W/m·K. Freezing and thawing temperature was applied on the four boundaries and heat convection took place between the boundary medium and the reinforced concrete beam. It should be noted that in the experiment, the beam was frozen in air while thawed in water according to ASTM C666-B method. Similarly, the boundary medium was chosen as air and water (heat convection coefficients of 15 and 200 W/m²·K) for freezing and thawing branch, respectively. For one FT cycle, in air-freezing phase the ambient temperature was decreasing from 5 °C to -18 °C gradually in 7 hours. While in water-thawing phase the water of 5 °C was kept supplied for 7 hours as the experimental conditions. **Fig. 5.1(b)** illustrated the counter map of temperature distribution at the end of air-freezing phase of the first FT cycle (7 hours) and from which it clearly indicated the thermal lag effect from heat

transfer during FTC. Temperature history of three different positions (corner, mid-point of top boundary and center) was plotted with ambient temperature variation, see **Fig. 5.2**. It yielded the minimum temperature of FTC was different due to the thermal lag effect, which would affect the calculation of material and bond deterioration. The cross-section of the RC beam was roughly divided into 6 regions, e.g. A-F in **Fig. 5.1(a)**. The minimum temperature of reach region was given by the average value of all the nodes it covered, which was also listed in **Table 5.1**. The material and bond deterioration were determined according to the minimum temperature of corresponding region, which would be stated in the following.

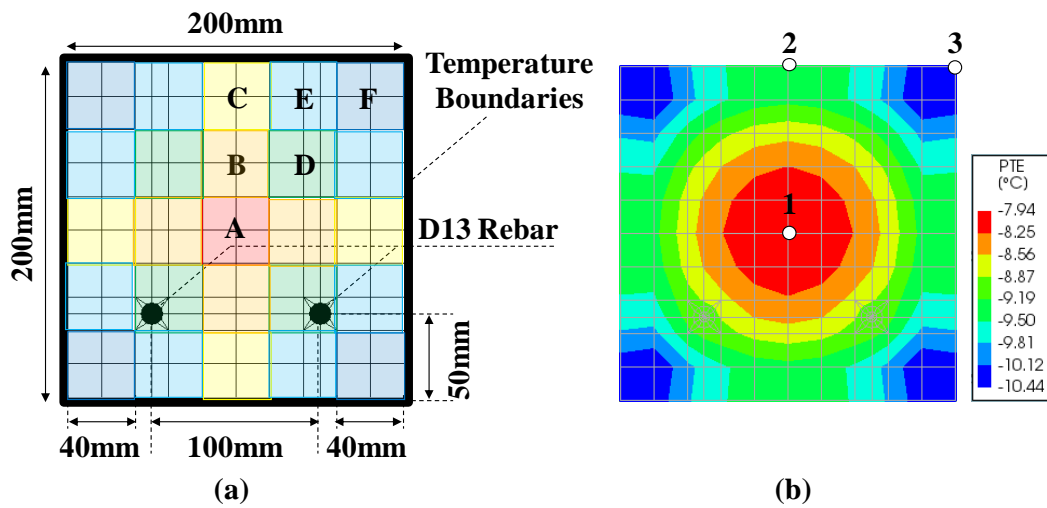


Fig. 5.1. (a) 2D heat transfer model (b) temperature contour map at 7 hours

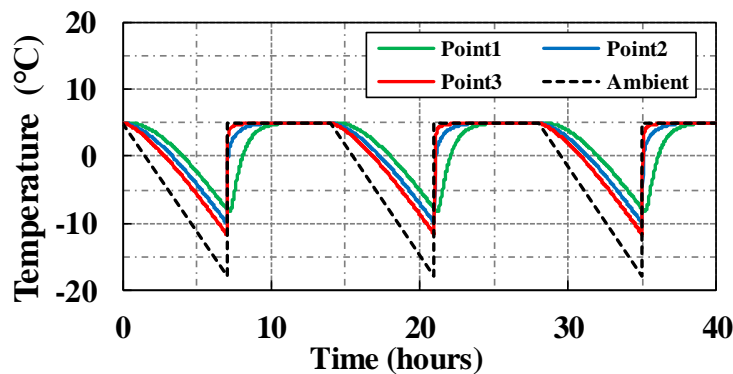


Fig. 5.2. Temperature history of different locations (3 FTCs)

5.1.2 3D reinforced concrete beam model

Combing the temperature history of different regions, analytical models of frost-damaged concrete (chapter 3) and bond behavior (chapter 4), 3D structural analysis was conducted with DIANA FEA (version 10.2). The reinforced concrete beams were modeled as: the cross-section of the model was $200 \times 200 \text{ mm}^2$ and length was 1600 mm (span length=1200 mm). Steel loading plate and supporting plates with dimension of $40 \times 40 \times 200 \text{ mm}^3$ were set at specific location to avoid the stress concentration, as shown in **Fig. 5.3**. Two longitudinal D13 rebars were modeled with bond-slip truss element and the location of the rebars was drawn in **Fig. 5.1(a)**. Concrete was modeled with solid element with mesh of $40 \times 40 \times 40 \text{ mm}^3$, see **Fig. 5.3**. The load type is prescribed displacement with 0.1 mm/step, which was applied vertically at the central line of loading plate while the restraint type was simply-supported, see **Fig. 5.3**.

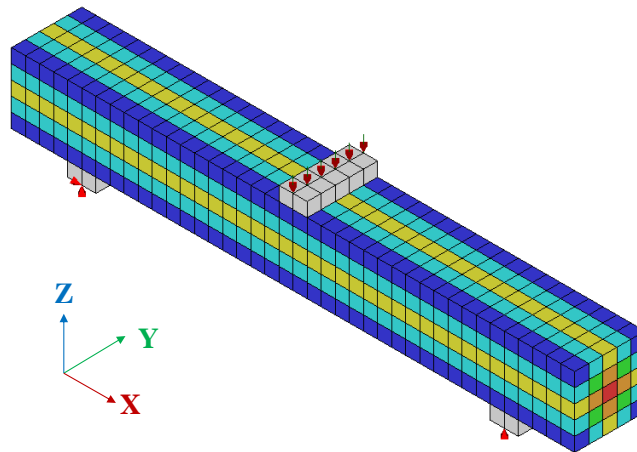


Fig. 5.3. Schematic of reinforced concrete beam (“T”) model

5.1.3 Material models

The material properties for non-damaged concrete were given as following: the compressive strength of intact concrete was 22.7 MPa, which was measured value in the verification experiment. The value of elastic modulus (E), compressive peak strain (ϵ_c) and tensile strength (f_t) were not measured in test, the values of these parameters were calculated based on some

recommendations. For instance, according to JSCE Standard Specifications for Concrete Structures, the elastic modulus and tensile strength could be calculated according to the compressive of concrete. Besides, Nicolo et al. (1994) proposed a relationship between the compressive strength of intact concrete and the strain at peak compressive stress. These equations were summarized in Eq. (5.1) and the calculated results were listed in **Table 5.1**. Parameters a and b for determining the compressive constitutive relationship of sound concrete were calculated by linear interpolation from the data of Guo et al. (2003), see **Table 5.1**. The maximum crack width of sound concrete was calculated based on the fracture energy and tensile strength. After all the parameters had been confirmed, the compressive and tensile constitutive relationship for sound concrete were given in **Fig. 5.4** and **5.5**. Total-strain-based crack model was adopted for concrete and the shear retention was modeled by introducing the shear retention factor. Mass of studies had yielded the shear retention factor was valued 0 to 1 and in the current study 0.5 was selected.

$$\begin{aligned}
 E &= \left(2.2 + \frac{f_c - 18}{20} \right) \times 10^4 \\
 f_t &= 0.23 (f_c)^{2/3} \\
 \varepsilon_c &= 1.491 \times 10^{-5} \cdot f_c + 0.00195
 \end{aligned} \tag{5.1}$$

For frost-damaged concrete at different locations (A-F), the damaged compressive strength was predicted by Eq. (3.7) and the other corresponding material parameters were calculated according to Eq. (3.8), (3.11), (3.9) and (3.13), as shown in **Table 5.1**. Afterwards, the compressive and tensile constitutive laws for frost-damaged concrete in different locations could be given according to Eq. (3.10) and (3.12), as shown in **Fig. 5.4** and **5.5**. Hanjari et al. (2013) mentioned in their study that the compressive stress-strain relationships in FEM analysis must be modified according to the dimension of specimens in material test and element size. In current study, the dimension of specimens was 200 mm as the RBSM model in section 3.1 and element size of concrete in FEM was 40 mm. As a result, the compressive constitutive relationships were calibrated and plotted together with the original curves, as shown in **Fig. 5.4**. The curves were named as “N/T-O/M-A~F” in which “N” and “T” represented sound and frost-damaged case; “O” and “M” stood for original and modified curves; “A~F” meant the regions as shown in **Fig. 5.1(a)**.

For reinforcement, the elastic modulus ($E_s=200$ GPa) and yielding strength ($f_y=370$ MPa) were determined based on the measurement in the verification experiment. Owing to localized yielding at the crack vicinity and bond effect, the yielding strength of reinforcement was reduced as suggested by Salem and Maekawa (1999), see Eq. (5.2). In Eq. (5.2), f_{y0} was the reduced yielding strength; f_t was the tensile strength of concrete and ρ represented the reinforcement ratio. After yielding, secondary hardening was considered with stiffness (E_s') of 0.01 times of E_s , as shown in Fig. 5.6.

$$f_{y0} = f_y - \frac{f_t}{2\rho} \quad (5.2)$$

Table 5.1. Material characteristics of sound and damaged concrete for FEM analysis

<i>Type</i>	<i>T</i> _{min} (°C)	<i>f</i> _c (MPa)	<i>E</i> (MPa)	<i>f</i> _t (MPa)	<i>ε</i> _c (μ)	<i>a</i>	<i>b</i>	<i>w</i> _{max} (mm)
Sound	/	22.70	24350	1.84	2288	2.10	0.99	0.36
Damaged-A	-8.35	13.49	11322	0.66	3459	0.63	2.12	1.26
Damaged-B	-8.47	13.35	11155	0.66	3477	0.62	2.13	1.27
Damaged-C	-9.31	12.40	10017	0.60	3598	0.56	2.19	1.34
Damaged-D	-8.81	12.96	10679	0.63	3527	0.59	2.16	1.30
Damaged-E	-9.62	12.07	9633	0.58	3640	0.54	2.21	1.36
Damaged-F	-10.47	11.22	8661	0.54	3748	0.50	2.26	1.42

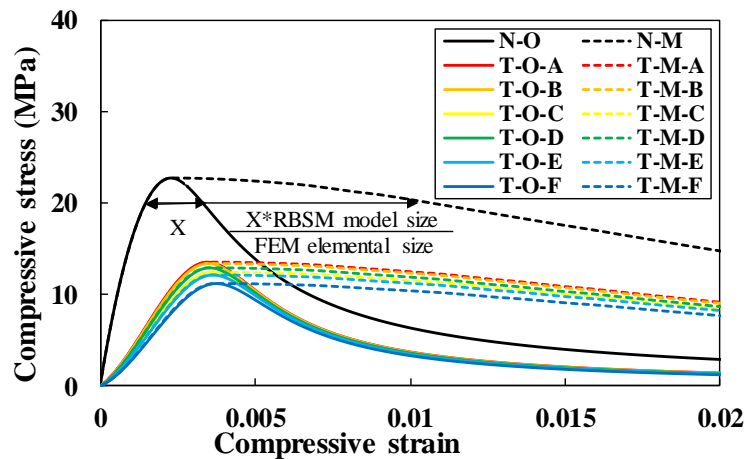


Fig. 5.4. Compressive stress-strain relationships of concrete

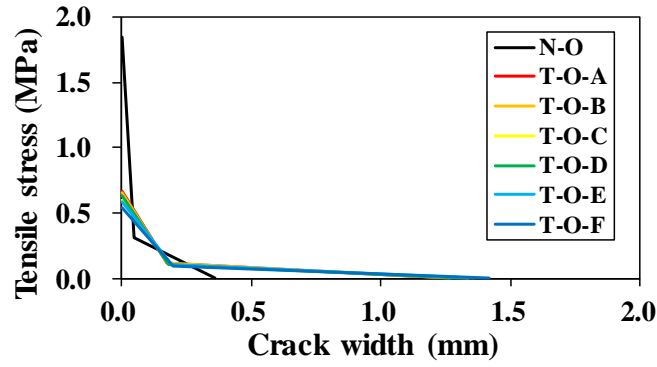


Fig. 5.5. Post-peak tensile stress-strain relationships of concrete

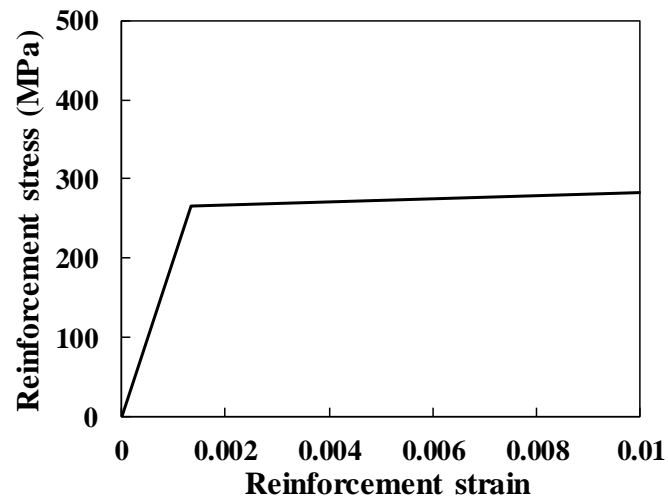


Fig. 5.6. Stress-strain relationship of reinforcement

5.1.4 Bond-slip models

According to fib Model Code 2010, the bond strength τ_l , residual bond strength τ_3 and corresponding slip values (s_1 , s_2 and s_3) for non-damaged RC beam could be calculated since the compressive strength of sound concrete had been provided. Together with the compressive strength of frost-damaged concrete in bond region and Eq. (4.14), the bond strength τ_{ld} , residual bond strength τ_{3d} for frost-damaged RC beam could also be given. The bond-slip relationships for both beams were plotted in **Fig. 5.7** where “N” and “T” represented the reference beam and the frost-damaged beam, respectively.

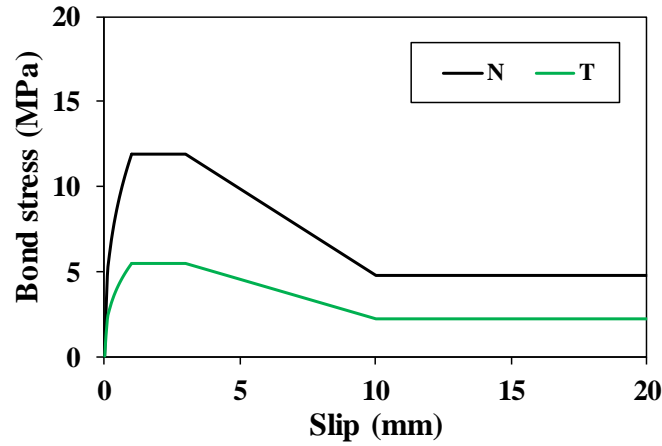


Fig. 5.7. Bond-slip relationships of sound and frost-damaged RC beam

All the constitutive models that would be adopted in the intact and frost-damage RC beam included compressive and tensile stress-strain relationship of concrete, stress-strain relationship of reinforcement, bond-slip behaviors between rebar and concrete. These models were directly integrated into the 3D RC beam model with DIANA FEA after which external loading was applied. Thus, the proposed multi-scale structural evaluation method could be summarized as: the deteriorated constitutive relationships including concrete materials and bond-slip properties were calculated based on the models proposed by 2D and axisymmetric mesoscale Rigid Body Spring Method simulations. Besides, the heat flow and temperature history during FTC was simulated by 2D FEM analysis. Finally, applying the deteriorated constitutive relationships into 3D FEM RC beam model with consideration of the non-uniform damage level, the structural analysis was conducted.

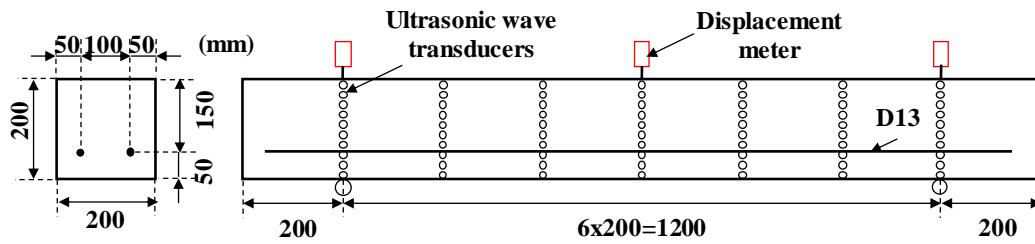
5.2 Experimental Verification

5.2.1 Specimens preparations

In order to verify the multi-scale evaluation method, experiment was executed by the cooperation member in Civil Engineering Research Institute of Japan. Two RC beams, naming after “N” and “T” which represented the reference case and frost-damaged case, and several cylindrical concrete specimens were casted. The cross-section of beams was 200x200 mm² and length was 1600 mm (span length=1200 mm). Concrete was made with Ordinary Portland Cement, river sand and crushed stones. The water cement ratio was set 0.65 to achieve an

accelerated degradation from freezing and thawing cycles and no air-entraining agent was added. For each beam, two D13 reinforcements with yielding strength of 370 MPa were embedded with depth of covering concrete equaling to 50 mm, as shown in **Fig. 5.8**.

As the frost damage indicator in the multi-scale methodology, the compressive strength of concrete was measured with the $\Phi 100 \times 200 \text{ mm}^2$ cylindrical concrete specimens. However, the compressive strength of concrete in RC members was somehow difficult to test for those in-service constructions. Some researchers suggested to relate ultrasonic pulse velocity with frost-damaged compressive strength of concrete. In this experiment, the cylindrical specimens suffered same FTC process as the RC beam and UPV was measured for both cylinder and RC beam for two reasons: 1. the relationship between ultrasonic wave velocity and compressive strength of frost-damaged concrete could be developed for evaluating the in-service structures; 2. the compressive strength of frost-damage RC beam predicted by the multi-scale methodology could be further verified.



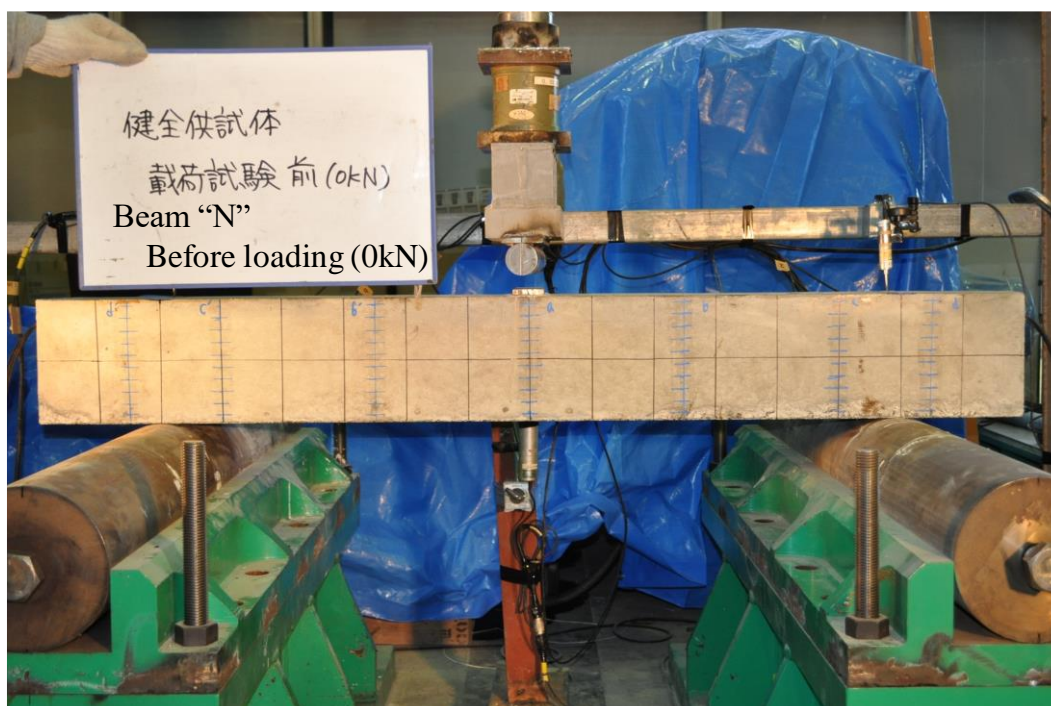


Fig. 5.8. Configuration of the RC beam and loading apparatus

5.2.2 FTC and loading

The cylindrical concrete specimens and beam “T” was put into the FTC set-up after they were cured in constant temperature and humidity for 28 days. The FTC set-up included a large temperature chamber containing a water pool made of steel framework with water resistant membrane covered in the inner surfaces. All the specimens were frozen in air and thawed in water as suggested by ASTM C666-B method. Pipes were used to connect the water pool and the water pumps. The pumps were controlled following the freezing and thawing system of the temperature chamber: during the thawing process, water with maximum temperature would be poured by one pipe into the pool where the specimens located for 7 hours. During this phase, the ice in specimens would melt and water was continuously absorbed by the specimens so that a high saturation degree could be assured for the next air-freezing phase; Then before freezing process started, the water inside the pool would be drained out by another pipe. In freezing phase, the ambient temperature gradually decreased from 5 °C to -18 °C in 7 hours.

UPV (ultrasonic pulse velocity) were firstly measured for cylindrical concrete specimens after they had suffered certain FT cycles. The FTC was finally ended after 300 cycles for beam

“T”. The UPV transducers (28 Hz and 1 kV) were put along the longitudinal direction of cylindrical specimens. After UPV measurement, the concrete specimens were conducted with uniaxial compression test so that the relationship between UPV and compressive strength could be derived. Meanwhile, the measurement of UPV for RC beam was parallelly along interval of 20 mm in height at different cross-sections, as shown in **Fig. 5.8**. After the UPV test, 3-point bending test was applied for both beam “N” and “T”. The loading apparatus of beam “N” was shown in **Fig. 5.8**.

5.3 Results and Discussions

5.3.1 Ultrasonic pulse velocity

The results of ultrasonic pulse velocity and compressive strength of frost-damaged concrete were drawn in **Fig. 5.9**. Normalized formulation was expressed to derive the empirical relationship between the normalized compressive strength (f_{cd}/f_c) and relative UPV (v_d/v), as Eq. (5.3). It could be indicated by the test results that the frost damage led to obvious reduction of pulse velocity, which was attributed to the cracks of concrete induced by frost action. As widely accepted, the transmission time was longer in crack (filled with water or air) compared with intact porous medium.

$$\frac{f_{cd}}{f_c} = 0.908 \frac{v_d}{v} + 0.092 \quad (5.3)$$

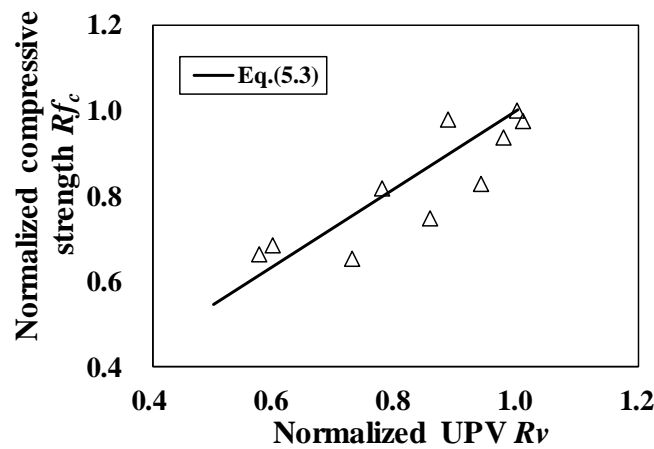


Fig. 5.9. UPV versus compressive strength of concrete (in normalized formulation)

The value of UPV of RC beam (both “N” and “T”) was plotted in **Fig. 5.10**. It yielded that the UPV for intact concrete was around 4.1 km/s while the value for concrete after 300 FTC decreased to 2.1 km/s. As shown in **Fig. 5.10**, the bottom area of beam “T” (0-70 mm in height) showed slightly higher UPV than other regions. The reason was that the ultrasonic pulse transmitted faster in those zones owing to the presence of reinforcement. In addition, the reinforcement restrained the surrounding concrete from expansion during FTCs which lead to less cracks and thus higher UPV. Based on the measured UPV values of beam “T” and the relationship between UPV and compressive strength of frost-damaged concrete (Eq. (5.3)), the averaged compressive strength of frost-damaged concrete (beam “T”) along height domain was calculated, referring to the triangle mark “Test” plotted in **Fig. 5.11**. As comparison, the averaged compressive strength from prediction by the multi-scale methodology in **Table 5.1** was also plotted (see the square mark “Prediction”) in **Fig. 5.11**, from which satisfactory agreement was found to further demonstrate the reliability of the proposed approach.

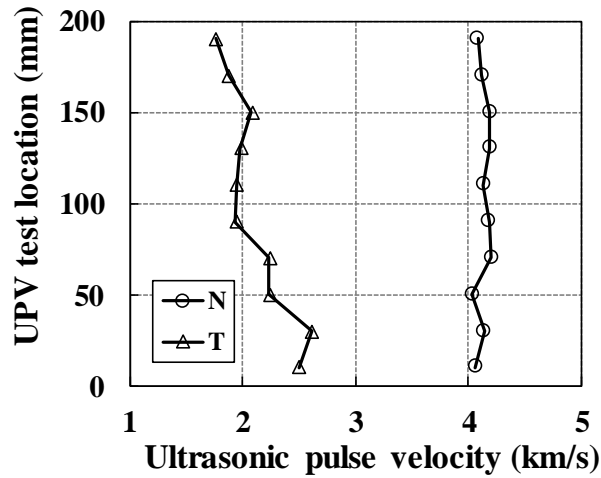


Fig. 5.10. UPV test result for beam “N” and “T”

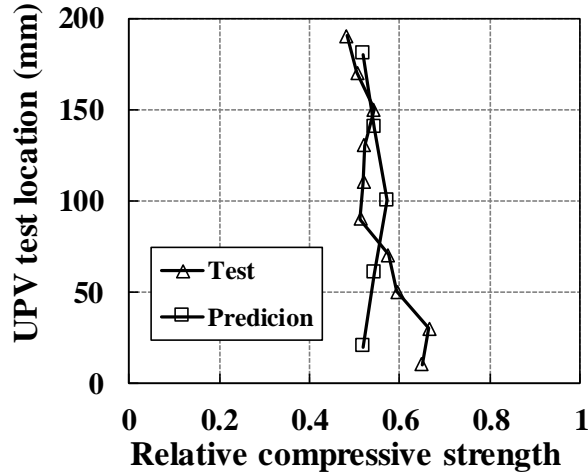


Fig. 5.11. R_{fc} by UPV test and prediction

5.3.2 Structural behaviors

The load-displacement curves for beam “N” and “T” by both experiment and FEM analysis were drawn in Fig. 5.12 and 5.13. For beam “N” as shown in Fig. 5.12, “EXP” and “SIM” meant the results by experiment and FEM analysis, respectively. Besides, for non-damaged beam, calculation results of cracking and yielding load as well as deflection based on theory of structural mechanics were also plotted, see the blue curve “CAL” in Fig. 5.12. It should be noted that the yielding deflection of beam “N” was calculated by adopting the minimum cross-sectional stiffness (mid-span) as the averaged value for the whole beam. According to Guo et al. (2003), this simplification would lead to overestimating of the yielding deflection but within 10% which was acceptable. In Fig. 5.12, the FEM numerical results indicated that the cracking load (9.98 kN) took place at deflection of 0.12 mm and the calculated results showed that the cracking load (8.72 kN) happened at deflection of 0.09 mm. In addition, yielding load was 40.86 kN at 1.70 mm and 43.93 at 1.94 mm from FEM numerical and calculated results. However, the experimental results showed larger deflection at yielding load (around 4 mm) compared with both numerical and calculated result, see Fig. 5.12.

For beam “T” as shown in Fig. 5.13, the FEM numerical results demonstrated that the cracking load (2.12 kN) and yielding load (35.85 kN) took place at deflection of 0.15 mm and 3.6 mm. The FEM numerical results showed satisfactory agreement with the experimental result

which strongly proved the reliability of the proposed methodology. From both numerical and experimental results, the frost-damaged beam performed smaller cracking and yielding load while as the deflection at yielding load increased on contrast with the non-damaged case. As a result, the stiffness of the frost damaged beam was reduced significantly.

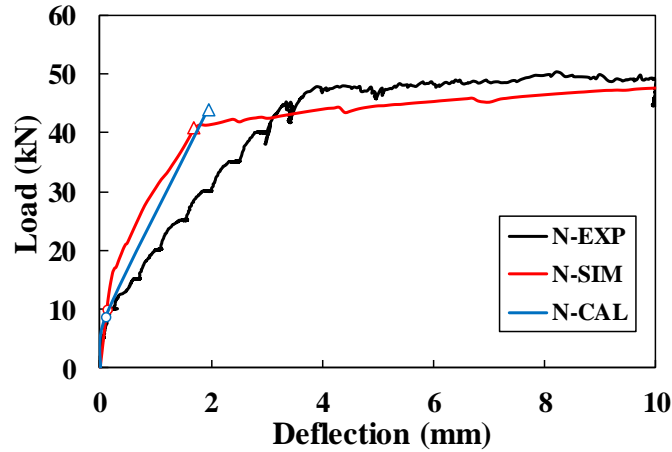


Fig. 5.12. Load-displacement curve by FEM analysis and experiment (N)

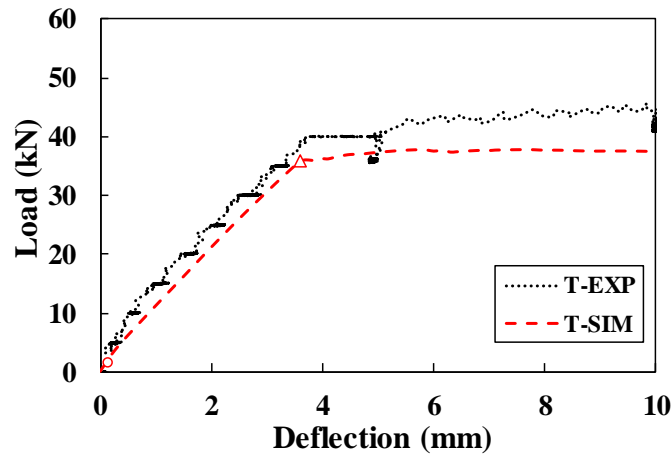


Fig. 5.13. Load-displacement curve by FEM analysis and experiment (T)

For beam “N” in the experiment, around nine flexural cracks with interval of 10 cm were observed at range of -50 to 30 cm from mid-span when reinforcement yielded, see the grey lines in **Fig. 5.14**. The crack patterns from FEM analysis at same status were also plotted in **Fig. 5.14** where the similar cracking patterns had been simulated, see the color lines. With increasing load in the experiment, maximum load of 61.1 kN was reached at deflection of 52mm. Meanwhile, the three cracks at -17, -80 and +15 cm from mid-span became wider as the black

lines in **Fig. 5.14**. Especially, the cracks at -17 and +15 cm from mid-span propagated along the tensile reinforcement if load increased further, and then load decreased rapidly which lead to the final failure of beam “N”, as shown in **Fig. 5.15**.

For beam “T” in the experiment, four flexural cracks with interval of 12 cm initiated at range of -15 to 20 cm from mid-span, as shown by the grey lines in **Fig. 5.16**. It should be noted that the heights which cracks reached at yielding load for beam “T” were somehow lower than that for beam “N”. As load increased to the maximum value, the flexural crack at -14 cm extended diagonally, which pointed from loading point towards -25 cm at the bottom surface, as shown by the black lines in **Fig. 5.16**. Besides, two short cracks initiated at -37 and +37 cm at the same time. The maximum load of frost-damaged beam “T” was 49.3 kN which was 19% less than that of beam “N”. Deflection at maximum load of beam “T” was 26.3 mm which was almost half compared with that of beam “N”. With further increasing load after maximum load had been achieved, the diagonal cracks propagated quickly from the loading point to the tension side of the beam, which lead to failure of beam “T”, as shown in **Fig. 5.17**. This could also be predicted from FEM numerical results shown in **Fig. 5.16** where many tiny diagonal cracks already took place at yielding load. Since no stirrups were provided in this study, the RC beams after suffering to frost action tended to initiate diagonal cracks easily due to the significantly reduced tensile strength. As a result, the failure mode of the frost-damaged RC beam turned out to be more brittle on contrast with the sound beam.

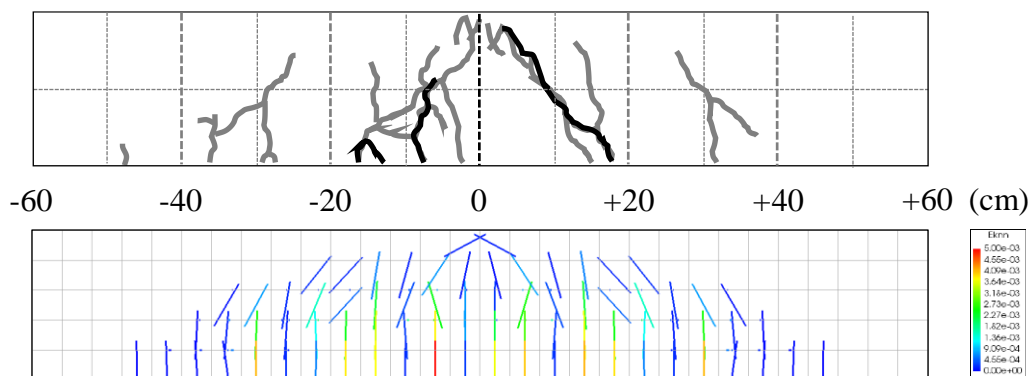


Fig. 5.14. Cracking patterns at yielding/maximum load of beam “N” by FEM



Fig. 5.15. Cracking patterns at failure stage of beam “N” by test

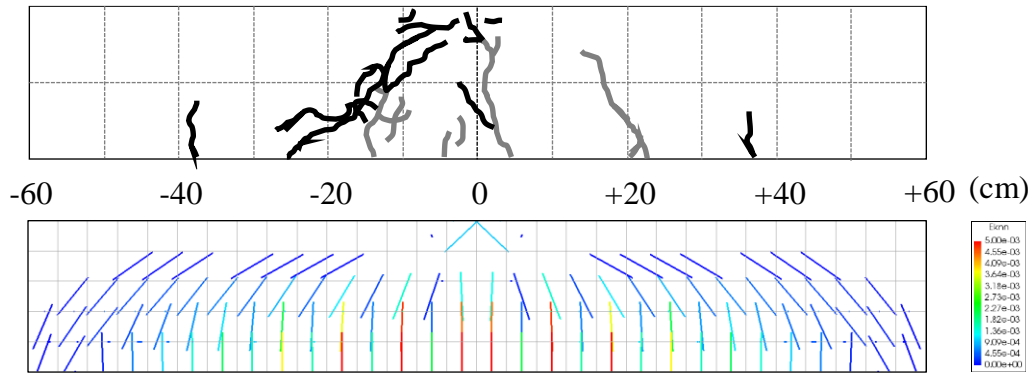


Fig. 5.16. Cracking patterns at yielding/maximum load of beam “T” by FEM

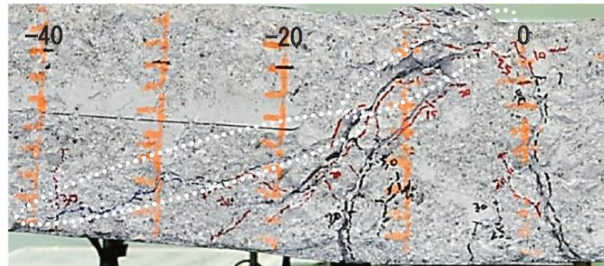


Fig. 5.17. Cracking patterns at failure stage of beam “T” by test

5.4 Conclusions of This Chapter

- (1) The proposed prediction models of frost-damaged concrete and bond constitutive laws by mesoscale RBSM was not only verified by available material tests (in chapter 3 and 4) but also proved to be adoptable for structural analysis with FEM in current chapter.
- (2) The deterioration laws of different regions were calculated with consideration of thermal history and distribution during FTC. The predicted compressive strength of concrete was verified using Ultrasonic Pulse Velocity measurement.

(3) Satisfactory agreement was achieved between the 3D FEM structural analysis and experiment, which both indicated that frost action would result in significant reduction of stiffness and strength of RC beam. Besides, the frost damage would change the failure mode in a certain extent where the RC beam tended to initiate more diagonal cracks after affected by frost action.

(4) The multi-scale structural evaluation methodology (chapter 3, 4 and 5) is effective to predict and evaluate the structural behaviors of RC members under the effect of frost damage. But due to the limitation of test data, whether it could be adopted as general method still need more evidence (experimental works and parametric studies), which is one of the future plans.

References

- Z. Wang, F. Gong, D. Zhang, H. Hayashida, T. Ueda, Mesoscale simulation of concrete behavior with non-uniform frost damage with verification by CT imaging, *Construction and Building Materials*. 157 (2017) 203-213.
- Diana finite element analysis, User's manual-release 10.2, Delft: TNO Building and Concrete Research. (2018).
- American Society for Testing and Materials Committee, Standard test method for resistance of concrete to rapid freezing and thawing (ASTM C666-15), West Conshohocken: ASTM International. (2015).
- Japan Society of Civil Engineers, Standard specifications for concrete structures, Tokyo: JSCE. (2007).
- B. De Nicolo, L. Pani, E. Pozzo, Strain of concrete at peak compressive stress for a wide range of compressive strength, *Materials and Structures*. 27 (4) (1994) 206-210.
- Z. Guo, X. Shi, Reinforced concrete theory and analysis, Beijing: Tsinghua University Press. (2003).
- K.Z. Hanjari, P. Kettil, K. Lundgren, Modelling the structural behavior of frost-damaged reinforced concrete structures, *Structure and Infrastructure Engineering*. 9 (5) (2013) 416-431.
- H. Salem, K. Maekawa, Spatially averaged tensile mechanics for cracked concrete and reinforcement under highly inelastic range, *Journal of Materials, Concrete Structures and Pavement*. 613 (42) (1999) 277-293.

Chapter 6

6. Conclusions

A multi-scale structural evaluation methodology on RC members under the effect of frost damage is proposed and discussed in this dissertation. The conclusions are summarized and remaining tasks are also presented:

- (1) The multi-scale method follows the procedure of “(micro-meso-macro) material-structural”. Start from explaining the physical models of ice strengthening/damaging effects in microscale, these effects are upscaled into the enhanced elastic properties and pre-stress of mesoscale springs in Rigid Body Spring Model. Meso-cracks and the deteriorated macroscale properties were achieved through numerical simulation. Macroscale degradation models including concrete and bond were proposed based on the meso-macro simulations. Together with the heat transfer analysis, the degradation models were implemented into FEM application and structural behaviors of RC member were analyzed.
- (2) 2D mesoscale plane stress RBSM was used for simulation and modeling of frost-damaged concrete. A prediction model of damaged compressive strength was proposed with verification by test results. Taking the relative compressive strength as the damage index, other material parameters were modeled, e.g. elastic modulus, peak strain, tensile strength, etc. The full constitutive curves including compression and tension were also presented and proved by various experiments.
- (3) Axisymmetric mesoscale RBSM was developed to simulate and model the frost-damaged bond properties. The stiffness matrix was derived and applied into the program. The reliability was demonstrated by conducting uniaxial compression of concrete, uniaxial tension of reinforcement as well as the pulling-out of reinforced concrete specimens. The effect of frost damage on bond properties was successfully simulated and the damage model was finally proposed.
- (4) Based on the 2D heat transfer analysis by FEM, the frost-damaged concrete and bond models were adopted in 3D RC beam model in macroscale. Structural analysis and experiment were conducted where satisfactory agreements could be found. Besides, ultrasonic pulse velocity test was conducted for both concrete and RC beam. With aid of

the relationship between Ultrasonic Pulse Velocity and damaged compressive strength, the applicability of multi-scale methodology was further demonstrated.

Future tasks:

- (a) In the future, parametric study is hopefully to be conducted with the proposed multi-scale structural evaluation method. With considering various environmental cases, the RC structural behaviors will be analyzed. Furthermore, the current design codes are aimed to be modified with respect to the effect of frost damage as deterioration factor.
- (b) Current methodology has already taken the heat transfer of RC member into consideration, as stated in section 5.1.1. However, not only heat transfer but also moisture transfer happens in mass construction and they are usually coupled with each other. Thus, the frost damage distribution in the structures might be affected by the coupled heat and moisture transfer. More precise evaluation of structural behaviors will be developed by combining the coupled transfer with frost damage in reinforced concrete structures.
- (c) In current study, the damaging effect due to frost action is considered as the meso-cracks induced by effective internal pressure by ice formation. However, there are also some micro-cracks initiated inside the RVE, which will affect the mesoscale properties. Such sort of microscale damaging effect is not modeled and integrated into the multi-scale evaluation method. In the future, this effect is aimed to be modeled theoretically and applied into RBSM, or with the aid of a microscale analytical application.
- (d) Actually, due to the existence of reinforcement, initial deformation (strain) is induced in the RC members before external loading is conducted. Such initial deformation will affect the results of structural evaluation, which has not been considered yet. In the future, the initial deformation (strain) will be calculated by RBSM and considered as the pre-deformed/loaded condition in FEM.

Appendix-A

Appendix-A

In appendix-A, the simulation of pulling-out test with 2D was presented, so that the importance of developing axisymmetric RBSM program could be understood better. Fig. A1 showed the pulling-out model with 2D RBSM. It could be observed that the 2D model behaved like a “sandwich” where the concrete and reinforcement were simply attached to each other. During the pulling-out process, the diagonal mechanical interlocking force (blue arrow) between ribs and concrete could be divided into the vertical (yellow arrow) and horizontal stress component (red arrow), see **Fig. A1**. The horizontal stress component could push the connecting concrete to move away towards the reinforcement. This movement should be confined by the hoop force of concrete ring (black arrow), which could not be considered in the 2D RBSM simulation. In addition, the moment induced by the horizontal stress component and reaction stress from bottom boundary will lead to rotation of the concrete cover. Thus, diagonal crack was observed in the simulation which was contradictory to the reality, as the blue oval showed in **Fig. A1**.

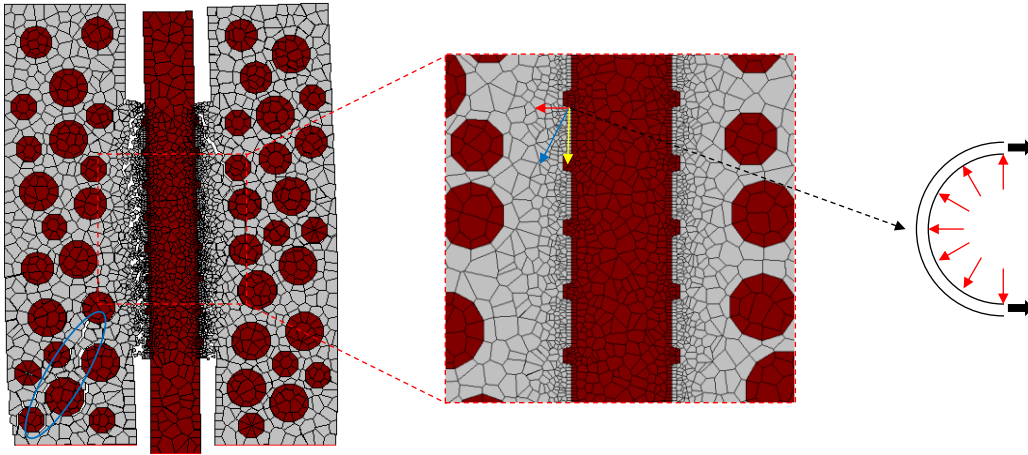


Fig. A1. Pulling-out simulation with 2D mesoscale RBSM

As a result, 2D mesoscale RBSM can no longer be adopted to simulate the pulling-out behaviors. The best solution is to use the 3D program. However, extreme computation time is needed for the 3D mesoscale simulation, especially when the frost damage process is simulated.

Appendix-B

Appendix-B

In appendix-B, the effect of elemental size on the pulling-out behaviors was discussed. As stated in section 4.3.1, the Voronoi element of mortar near bond interface was meshed gradually from 0.5 to 2 mm. Here several cases were simulated by changing the elemental size in the bond region: as shown in **Fig. B1**, the mortar elements attached to reinforcement were set constantly with dimension of 0.5 mm. However, the gradient factor (elemental size of layer n /elemental size of layer $n-1$) varied to be 1.1, 1.2, 1.5 and 1.8 for models (a)-(d). All the other material properties were same including the embedment length, concrete strength, etc.

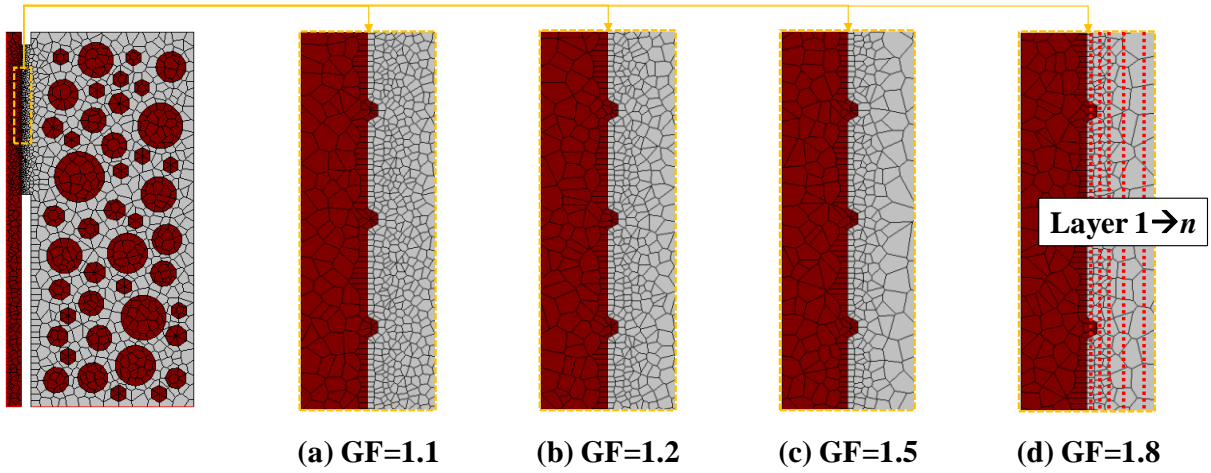


Fig. B1. Illustration of model with different gradient factors

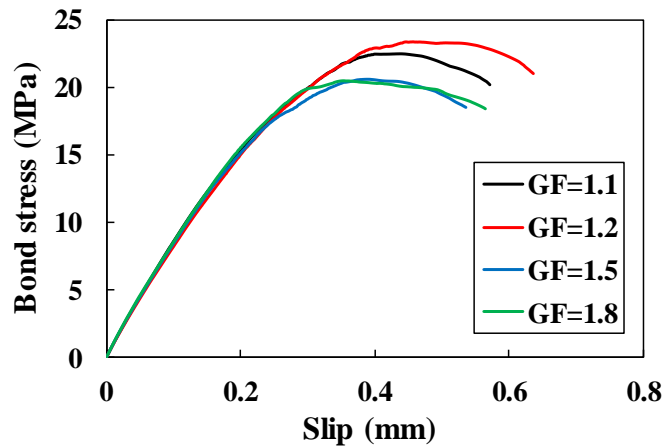


Fig. B2. Bond-slip behaviors with different gradient factors

The simulation results of bond-slip behaviors for all the models were plotted in **Fig. B2**. It could be seen that if mesh of mortar was finer in bond region, the calculated bond strength tended to be larger and the corresponding slip was also larger. The maximum and minimum bond strength simulated by different models were 23.38 and 20.47 MPa, respectively. The scattering was limited within 14.2% by different mesh types (gradient factors). Though finer mesh lead to a more precise simulation result, GF=1.5 was adopted in current study for consideration of the conservative prediction and less computation time consumption.